DEPARTMENT OF PHYSICS, UNIVERSITY OF JYVÄSKYLÄ
RESEARCH REPORT No. 7/2005

HYDRODYNAMICAL ANALYSIS OF HADRON SPECTRA AND THERMAL PHOTON EMISSION IN ULTRARELATIVISTIC HEAVY ION COLLISIONS

BY
SAMI RÄSÄNEN

Academic Dissertation
for the Degree of
Doctor of Philosophy

Jyväskylä, Finland
December, 2005

ISBN 978-951-39-3164-3
URN:ISBN:978-951-39-3164-3

Preface

The work reviewed in this thesis has been carried out during the years 2001-2005 in the Department of Physics at the University of Jyväskylä.

I am most grateful to my supervisors, Prof. Vesa Ruuskanen and Doc. Kari J. Eskola, for guidance and the invaluable opportunities that have become possible due to their continuous support during these years. Their knowledge in many fields of physics has been exemplary for me.

Staff and friends at the Department of Physics have created an inspiring and enjoyable atmosphere in which it has been a pleasure to work. I am also pleased about the many possibilities to teach in the department as I feel the calling to teach.

The financial support from the Graduate School of Particle and Nuclear Physics (GRASPANP) is gratefully acknowledged. I thank the Wihuri Foundation for funding my participation in the Quark Matter 2004 conference and the ECT* for the Marie Curie Fellowship, that gave me an opportunity to spend three memorable months at Trento, Italy, in 2002.

I thank David Agar for his assistance with the language of the manuscript. Any remaining mistakes in English grammar are, of course, to be considered as my negligence.

Finally, I wish to thank Katja and my parents for their love and support.

Jyväskylä, November 2005

Sami Räsänen

List of Publications

This thesis consists of an introductory part and of the following publications:

I Multiplicities and Transverse Energies in Central AA Collisions at RHIC and LHC from pQCD, Saturation and Hydrodynamics
K. J. Eskola, P. V. Ruuskanen, S. S. Räsänen and K. Tuominen,
Nucl. Phys. A **696** (2001) 715 [ArXiv:hep-ph/0104010].

II Photon Emission in Heavy Ion Collisions at the CERN SPS
P. Huovinen, P. V. Ruuskanen and S. S. Räsänen,
Phys. Lett. B **535** (2002) 109 [ArXiv:nucl-th/0111052].

III Dependence of Hadron Spectra on Decoupling Temperature and Resonance Contributions
K. J. Eskola, H. Niemi, P. V. Ruuskanen and S. S. Räsänen,
Phys. Lett. B **566** (2003) 187 [ArXiv:hep-ph/0206230].

IV On Hydrodynamical Description of Thermal Photons
S. S. Räsänen,
Nucl. Phys. A **715** (2003) 717c [ArXiv:nucl-th/0210007].

V Predictions for low-pT and high-pT hadron spectra in nearly central Pb+Pb collisions at s(1/2)(NN) = 5.5 TeV tested at s**(1/2)(NN) = 130 GeV and 200 GeV**
K. J. Eskola, H. Honkanen, H. Niemi, P. V. Ruuskanen and S. S. Räsänen,
Phys. Rev. C **72** (2005) 044904 [ArXiv:hep-ph/0506049].

The author has used an independent numerical code to check results in publication I and further developed the code to achieve results for publications II-V. The author has performed all boost-invariant calculations presented in paper II. In publications III and V the author has performed a considerable part of the numerical work and has written a significant portion of paper V. Publication IV is a review article, containing also some new results, written by the author.

Contents

Chapter 1

Introduction

Due to colour confinement, there are no free quarks in nature. However, shortly after the introduction of quarks, it was predicted [1, 2] that at sufficiently high temperatures or densities quarks and gluons would no longer be confined within hadrons. Instead, they could move freely within the hot or dense region. After this deconfinement transition, hadrons are no longer the relevant degrees of freedom in the matter. Instead, the properties of this new state of matter, which is named quark-gluon plasma (QGP) or quark matter, are dictated by the properties of the quarks and the gluons.

The theory that describes the strong interactions among quarks and gluons is called quantum chromodynamics (QCD). The thermodynamics of strongly interacting matter, currently at small net-baryon densities but over a large temperature range, can be studied in a non-perturbative fashion with numerical simulations of QCD on the lattice. Based on these studies, the deconfinement transition at the vanishing net-baryon density, takes place at the critical temperature $T_c \sim 150 - 180$ MeV[1] [3], which is roughly 10 000 times the temperature of the plasma in the fusion reactor. At low temperatures, the transition has been estimated to take place when the baryon density is a few times the nuclear matter density [4]. Both the high and low temperature cases correspond to an energy density of the order of GeV/fm^3. However, the phase diagram of the QCD in the low temperature and high baryo-chemical potential region has more structure than expected. In this region there are colour superconducting phases of the quark matter [5]. QGP exists also at high net-baryon densities but at finite temperature depending on the value of the baryo-chemical potential.

[1] If $k_B \equiv 1$, then the dimensions of temperature and energy are the same. For example, a temperature of 1 MeV $\approx 11.6 \times 10^9$ K.

The densities required for the transition to take place may exist in the cores of neutron stars [6, 7]. The temperature in the less than microsecond-old universe was high enough for matter to be in the QGP phase [8]. These are extreme conditions compared to those encountered in every day life and clearly, it is not possible to produce large amounts of quark matter in laboratory conditions. However, for a transient moment, similar densities can be achieved in an ultrarelativistic collision between two heavy nuclei. The major goal of relativistic heavy ion physics is to probe the phase diagram of the strongly interacting matter and to verify the existence of the chiral and deconfinement transitions.

The center-of-mass collision (CMS) energies achieved in fixed target experiments performed at the Brookhaven AGS (Alternating Gradient Synchrotron) and at the CERN SPS (Super Proton Synchrotron) were in the range $\sqrt{s_{NN}} \simeq 2 \ldots 17$ GeV. The formation of QGP may have taken place in the lead-lead collisions at the SPS but final conclusions are still under debate. The RHIC (Relativistic Heavy Ion Collider), located at Brookhaven National Laboratory, is a facility dedicated to the search for QGP. The maximum CMS energy in gold-gold collisions at RHIC is $\sqrt{s_{NN}} = 200$ GeV. Even higher CMS-energy, $\sqrt{s_{NN}} = 5500$ GeV, will be reached in lead-lead collisions at the CERN LHC (Large Hadron Collider).

At collider energies, at both the RHIC and LHC, the obtained energy densities are sufficiently high for the formation of QGP. Based on the Bjorken estimate [9], $\epsilon = \frac{dE_T}{d\eta}/(\pi R_A^2 \tau)$, and the measured transverse energy $dE_T/d\eta \sim 610$ GeV [10, 11], the initial energy density (at $\tau \sim 1$ fm/c) obtained at the RHIC energies is $\epsilon \sim 5$ GeV/fm^3, which is well above the critical energy density. However, one of the major open questions in this research field is whether or not the fireball produced in the collision thermalizes. This is an important prerequisite for formation of a quark-gluon *plasma*, instead of "merely" dense strongly interacting matter, in the heavy ion collisions.

Although the thermalization of the fireball has not yet been proven, there is a wealth of evidence supporting the existence of pressure within the fireball. In particular, the observed azimuthal asymmetry in the measured transverse spectra of hadrons in non-central collisions [12, 13, 14] could not be formed without frequent secondary interactions.

In hydrodynamical modelling of heavy ion collisions, the secondary interactions are assumed to lead to the local thermalization of the fireball. After the primary interactions have taken place, the fireball begins to expand, cool

and rarefy. During this evolution stage, which is described by the hydrodynamical evolution equations, collective flow is generated from the pressure gradients.

A plasma of quarks and gluons rehadronizes during the expansion stage as the temperature of the matter drops to T_c. After the expansion rate exceeds the scattering rate in the hadronic phase, the thermodynamical (kinetic) equilibrium is no longer maintained and the fireball breaks into freely streaming hadrons. This decoupling process is most likely gradual but often effectively described by assuming that the decoupling takes place on a hypersurface characterized by a constant temperature. These thermal hadrons are emitted in the late stages of the evolution and dominate the final hadron spectra in the region of low transverse momentum, p_T. Roughly 99 % of the final measured hadrons belong to this thermal region in which the spectra show a roughly exponential fall off. These abundant low-p_T particles form the bulk of produced final hadrons.

Initially produced partons having high transverse momentum are not expected to thermalize. Instead, they lose energy in traversing the dense medium formed by the softer particles. This energy loss, named jet quenching, is one of the predicted signals for the formation of QGP (see e.g. [15] for a recent review).

Electromagnetic emission, i.e. real photons and lepton pairs from the decays of virtual photons, from the secondary interactions provide an excellent probe for the dense medium because, due to their large mean free paths, they escape from the collision region without further interactions. In particular, the electromagnetic emission is sensitive to the early stages of the evolution.

In addition to photon emission, hadron multiplicities at RHIC and at the LHC energies were studied in this thesis using a hydrodynamical model. The initial state of the evolution is obtained from a perturbative QCD calculation with a conjecture of final state saturation [I]. The predictions of this framework, for the hadron spectra in the 5 % most central Au+Au collisions at $\sqrt{s_{NN}} = 130$ GeV [III] and $\sqrt{s_{NN}} = 200$ GeV [V], were compared with the data taken at the RHIC. Predictions for the hadron spectra in the 5 % most central Pb+Pb collision at $\sqrt{s_{NN}} = 5500$ GeV were also presented in [V]. The emission of thermal photons at the SPS energy was studied in [II] and the prediction for the RHIC energy was shown in [IV].

Chapter 2

Hydrodynamical Evolution

A dense and hot fireball of strongly interacting matter is created in the ultrarelativistic collision of two heavy nuclei. If the fireball reaches a local thermal equilibrium, after the particle production has taken place, the further evolution of the fireball can be described using hydrodynamics. The use of hydrodynamics has a long history dating back to 1950's [16], when it was applied to particle production in pp-collisions.

When applicable, the hydrodynamical description provides a relatively simple and concrete picture of the hot and dense stage of the evolution. It also enables the direct testing of the equations of state of strongly interacting matter and allows the use of familiar concepts, such as temperature and flow velocity, in the description of rarefaction and the cooling of the fireball.

However, particle production in primary interactions among the partons of incoming nuclei has to be modelled separately and one has to assume that secondary interactions occur frequently enough to lead to the local thermalization of the fireball. Thermalization is also assumed to be maintained throughout the evolution. In the chapters that follow the primary interactions, at collider energies, are described with a pQCD+saturation model [17]. Particle production and assumptions needed to construct the initial state, from which the hydrodynamical evolution begins, are discussed in Chap. 3.

In the following sections the main features of the hydrodynamical modelling of heavy ion collisions are reviewed.

2.1 Evolution equations

Hydrodynamical evolution equations express the conservation of energy and momentum

$$\partial_\mu T^{\mu\nu}(x) = 0, \tag{2.1}$$

where $T^{\mu\nu}$ is the energy-momentum tensor. For other conserved quantities $Q_i = \int d^3x J_i^0$, such as net-baryon number, a local current conservation equation,

$$\partial_\mu J_i^\mu(x) = 0, \tag{2.2}$$

is obtained. Equations (2.1) and (2.2) are general and independent of the dynamical properties of the system.

In order to proceed, it is further assumed that the matter behaves as an ideal fluid, in which case the energy-momentum tensor takes the form

$$T^{\mu\nu} = (\epsilon + P)u^\mu u^\nu - g^{\mu\nu}P, \tag{2.3}$$

where u^μ is the four-velocity of the flow of the fluid and ϵ and P are the energy density and pressure in the local rest frame (i.e. the co-moving frame) of the fluid. Here, the conservation of the net-baryon number is taken into account. With the four-velocity u^μ of the fluid, the net-baryon current (2.2) takes the form $J_B^\mu = n_B u^\mu$, where $n_B := \rho_B - \rho_{\bar{B}}$ is the local net-baryon density in the co-moving frame, that is the difference of baryon and anti-baryon densities ρ_B and $\rho_{\bar{B}}$. To close the conservation equations (2.1) and (2.2), an equation of state (EoS),

$$P = P(\epsilon, n_B), \tag{2.4}$$

which gives the pressure in terms of energy and net-baryon density, is needed. The ideal fluid approximation (2.3) means that the dissipative and viscous effects are neglected and the evolution is isentropic. Viscous effects have been recently studied in [18, 19, 20].

The whole collision process cannot be treated with hydrodynamics at ultra-relativistic energies. The primary interactions are not an equilibrium processes and they have to be modelled separately. The hydrodynamical model also cannot describe how and in which time scale, if any, the fireball reaches the thermal equilibrium. In the majority of hydrodynamical studies, the initial densities and velocity fields are described using phenomenological parametrizations at some finite (thermalization) time after the primary interactions have taken place. The choice of the initial state is not unambiguous since the final measured observables are reproduced equally well by

many different parametrizations. If a rapid thermalization is assumed, the pQCD+saturation model provides a closed framework for the description of the initial densities created in the central collisions at the collider energies obtained in RHIC and the LHC [I, III, IV, V]. However, the pQCD+ saturation approach, as discussed in Chap. 3, is not meaningful at lower energies. Thus parametrized initial states have to be used in the calculations at the SPS energies [II, IV].

Cooling and rarefaction of the fireball are dictated by the hydrodynamical evolution equations. As the fireball becomes dilute, the particles cease to interact and freely stream to the detectors. This freeze-out process is described in Sec. 2.5.

In the following sections particular solutions for the evolution equations will be discussed in order to illustrate what needs to be known about the initial state.

2.2 Boost-invariant solution for hydrodynamical equations

One-dimensional analytical solutions can be found for the continuity equations (2.1) and (2.2). A solution in the limit of infinite collision energy was obtained by Bjorken in 1982 [9]. In the Bjorken scenario two infinitely large nuclei, that are Lorentz contracted to thin plates, collide with ultra-relativistic energy. Bjorken's solution was generalized in [21, 22] for head-on (zero impact parameter) collisions of two heavy nuclei with a finite transverse size. The solution includes the transverse expansion but can no longer be solved analytically. Both solutions are based on an assumption, that the experimental observables do not depend on the rapidity, $y \equiv \frac{1}{2}\ln[(E+p_z)/(E-p_z)]$, around the mid-rapidity $y = 0$. This provides constraints on the four-velocity of the flow.

A head-on collision of two spherical nuclei is cylindrically symmetric and there is no dependence on the azimuthal angle ϕ in the transverse plane (xy-plane). Longitudinal boost-invariance requires the time and longitudinal components of the flow velocity u^μ to be proportional to t and z, respectively, with the same factor of proportionality. Also, the radial velocity v_r should be unaffected by the longitudinal Lorentz boost and thus, it can depend only on the proper time $\tau \equiv \sqrt{t^2 - z^2}$ and the transverse radius $r \equiv \sqrt{x^2 + y^2}$. With the normalization $u^2 = u_\mu u^\mu = 1$, in cylindrical

coordinates $x^\mu = (t, r, \phi, z)$, the four-velocity can be written as [22, 23]

$$u^\mu = \gamma_r \left(\frac{t}{\tau}, v_r(\tau, r), 0, \frac{z}{\tau} \right), \tag{2.5}$$

where $1/\gamma_r = \sqrt{1 - v_r^2}$. In terms of the space-time rapidity, $\eta_{\rm st} \equiv \frac{1}{2} \ln[(t + z)/(t - z)]$, Eq. (2.5) takes the form

$$u^\mu = \gamma_r (\cosh \eta_{\rm st}, v_r(\tau, r), 0, \sinh \eta_{\rm st}). \tag{2.6}$$

The concept of boost-invariance becomes now transparent. The space-time rapidity $\eta_{\rm st}$ is additive in the longitudinal Lorentz boosts and it can be seen directly from (2.6) that the description of the flow appears the same in every frame boosted from $z = 0 = \eta_{\rm st}$. Thus, the original (3+1)-dimensional problem is reduced to a (1+1)-dimensional one with the limitation that (formally) only ultra-relativistic head-on collisions of spherical nuclei can be considered and all information on the rapidity y is lost.

The initial conditions should respect the same symmetries. This means the energy- and baryon number densities,

$$\epsilon = \epsilon(\tau_0, r) \qquad \text{and} \qquad \mathrm{n_B} = \mathrm{n_B}(\tau_0, \mathrm{r}), \tag{2.7}$$

must be specified at some (finite) constant of proper time τ_0. In the case of longitudinal scaling flow, $v_z = z/t$, all particles can be traced back to the collision point $(t, z) = (0, 0)$. Thus, in the boost-invariant scenario, τ_0 uniquely defines the thermalization time. The concept of thermalization time becomes more involved when the assumption of boost-invariant flow is relaxed [IV, 24, 25].

The initial transverse velocity $v_r = v_r(\tau_0, r)$ also has to be specified, but it is always, unless stated otherwise, chosen to be $v_r(\tau_0, r) \equiv 0$. Within these choices, when τ_0, shapes and normalizations of $\epsilon(\tau_0, r)$ and $n_B(\tau_0, r)$ are specified, the deterministic evolution of ϵ, n_B and v_r follows from the numerical solution of the hydrodynamical evolution equations.

2.3 Relaxing the approximations of boost-invariance or cylindrical symmetry

Relaxing the assumption of longitudinal boost-invariant flow is, in principle, straightforward. The $\eta_{\rm st}$ in Eq. (2.6) should be replaced by a general longitudinal flow rapidity $\theta = \theta(\tau, r, \eta_{\rm st})$ and the transverse flow should be

allowed to also depend on $\eta_{\rm st}$ [23]. This was done in [24], where the authors discuss the hadron and electromagnetic spectra in S+Au collisions at the SPS.

When the initial densities and flow velocity also have to be specified in the longitudinal direction, the description of the initial state becomes more complicated [24, 25, 26]. There is considerable ambiguity in the choice of the initial state. References [25, 26] present a model based on the local nuclear thickness. In the model, the spatial energy and baryon number densities depend both on the equation of state and on the choice of the initial longitudinal velocity profile. At the SPS, the parameter space is still fairly large and various choices reproduce all hadron data equally well.

As discussed in [27], electromagnetic probes can provide more constraints for the initial state. This study was revised in [II] after the WA98 collaboration reported data on direct photons[1] measured in Pb-Pb collisions at the SPS [28, 29]. A comparison between boost-invariant and non-boost-invariant descriptions of the direct photon data was presented in [II]. The studies of the WA98 data were reviewed in [IV], where the role of the initial state was emphasized.

In the non-central collisions of spherical nuclei or in the central collisions of deformed nuclei, such as uranium, the initial fireball is almond shaped in the transverse plane. Deformation in the initial densities leads to steeper pressure gradients and hence a stronger flow into the short direction of the almond which is defined by the impact parameter. As a result of an anisotropic flow in the transverse plane, the final transverse spectra of hadrons are anisotropic [30]. The anisotropy is studied using Fourier decomposition of the azimuthal angle dependence in the final spectra. The second Fourier coefficient is called the elliptic flow. All odd Fourier coefficients vanish at mid-rapidity when symmetric AA collisions are considered [31]. Studies of the elliptic flow at RHIC are reviewed e.g. in [32].

The full complexity of ideal fluid hydrodynamics has been described by T. Hirano whose simulation software can model a (3+1)-dimensional space-time evolution [33]. Such an achievement opens the possibility to also study the rapidity dependence of e.g. multiplicities, transverse spectra and elliptic flow. However, the rapidity dependence of the elliptic flow, when the transverse spectra are simultaneously well described, is especially difficult to obtain [33, 34]. Additional research is needed to understand the elliptic

[1] Photons are discussed at Sec. 2.7.1.

flow within the fragmentation regions [35].

As will be presented in Sec. 2.6, at collider energies the more limited boost-invariant code used in calculations here is adequate to describe the transverse flow and transverse spectra of hadrons at mid-rapidity. As discussed above and in Chap. 3, a description for the initial state used here is obtained from a closed pQCD+saturation calculation [17]. Hirano and Nara have made [36] a fully (3+1)-dimensional hydrodynamical study where the initial state is based on the semi-analytical Colour Glass Condensate (CGC) model [37]. They obtain an excellent description of the rapidity dependence of charged particle multiplicities and transverse spectra of pions. However, the CGC model [37] leaves the normalization of the initial gluon density open. Hence, while the shape of the initial density in the hydrodynamical description [36] is obtained from a calculation, assuming that the shape does not change considerably in between formation and thermalization, the normalizations of initial densities, however, are determined by comparing the final results to experimental data. The initial net-baryon density can also be obtained from the pQCD+saturation model [17], as discussed in Chap. 3, while the CGC model [37] describes the initial gluon production only.

2.4 Equation of state

For many years, the thermodynamics of quarks and gluons and the transition between the low temperature hadronic phase and quark gluon plasma (QGP) has been studied within the framework of lattice regularized QCD. Knowledge of the high temperature phase, at vanishing baryo-chemical potential, has improved through the development in discretization schemes and increased computer resources [3].

Quark masses in (2+1)-flavour QCD, i.e. simulations with two light and one heavier quark, are too large to be compared to the realistic situation in nature. By extrapolation to the chiral limit, the critical temperature for two-flavour QCD is $167-181$ MeV, depending on the discretization scheme. A three-flavour QCD is found to lead to consistently lower values for the critical temperature, T_c(2-flavour)$-T_c$(3-flavour) ~ 20 MeV. The results obtained from calculations with (2+1)-flavours indicate that the critical temperature seems to be closer to the two than the three-flavour case.

The results obtained from the lattice calculation approach the free gas limit

for gluons and N_f massless quarks

$$\epsilon = 3P = \left(16 + \frac{21}{2}N_f\right)\frac{\pi^2}{30}\,T^4 \tag{2.8}$$

slowly and deviations are ~ 15 % when $T \sim (2-4)T_c$ [3]. Also, the order of the phase transition is still uncertain. Results from the two-flavour QCD, with a finite baryo-chemical potential, indicate, that there may be a tricritical point. If this was indeed the case, there is a first order phase transition above μ_c while below μ_c, there is a cross over transition [38].

The region $T \lesssim 0.9T_c$ of the EoS is the most difficult one to obtain from the lattice calculations. In the hydrodynamical studies it is also important to know, as discussed in Sec. 2.5, what exactly are the hadronic degrees of freedom at $T < T_c$. Therefore, the low temperature phase is described as a free gas of hadrons and resonances. A recent study [39] also indicates that the $T < T_c$ regime, obtained from the two-flavour lattice calculations, can be well described by a non-interacting hadron resonance gas model.

Details of the construction of the hadronic part of the EoS are presented in Ref. [24]. The hadron phase consists of all hadrons and resonances up to 1.4 GeV [I, II, IV] or 2 GeV [III, V] and matter is required to be strangeness neutral.

In order to construct an EoS, one possibility would be to describe the high temperature phase as a parametrization of the lattice results and to join this parametrization smoothly to the hadron resonance gas near the critical temperature. Fig. 2.1 shows ϵ/T^4 (solid line) and P/T^4 (dashed line) as a function of T/T_c in the EoS, where hadron resonance gas is joined to a parametrization obtained from a thermal quasi-particle description of lattice results [40]. The free gas limit, with $N_f = 3$, is indicated.

A detailed study [41], which uses the construction of the EoS as described above, shows that the transverse spectra of hadrons are fairly insensitive to the description of the phase transition region. A similar calculation, verifying the above statement, has been made by the author. Hence, here the use of the simpler bag EoS, with a first order phase transition between the ideal gas of quarks and gluons and a free gas of hadrons and hadron resonances, is justified. The bag constant is chosen such that the critical temperature $T_c \simeq 165$ MeV. The bag model equation of state (EoS A), where hadrons and resonances up to $m = 1.4$ GeV are included in the hadron resonance gas at $T < T_c$, is shown as the dotted and dashed-dotted

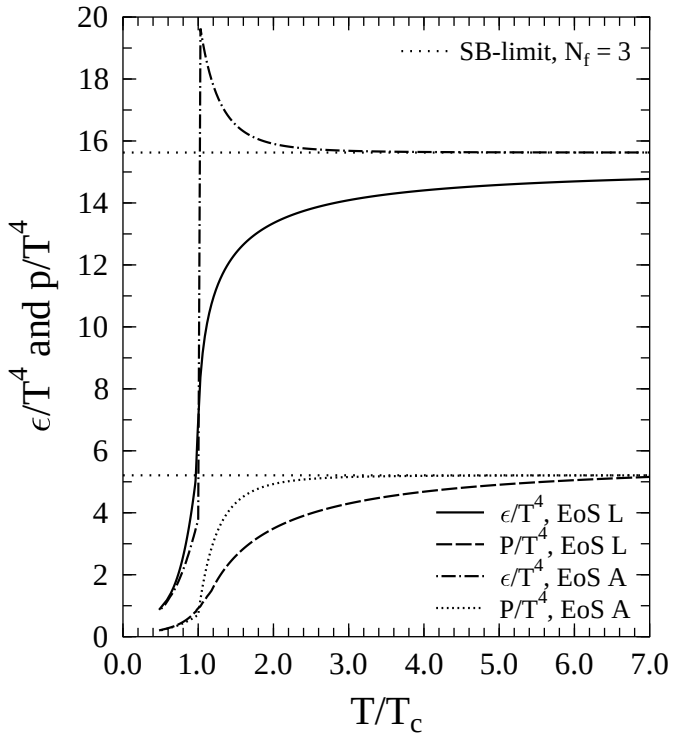

Figure 2.1: Energy density and pressure, illustrated as dimensionless quantities ϵ/T^4 and P/T^4, for the bag equation of state (EoS A) and hadron resonance gas + quasi-particle parametrization [40] of lattice results (EoS L).

lines in Fig. 2.1.

2.5 Decoupling and hadronic observables

Rarefaction and the cooling of the fireball is described with the hydrodynamic evolution equations. At some point, either the mean free path of particles become larger than size of the system or the expansion rate exceeds the interaction rate. As a result, the thermodynamical equilibrium ceases to exist and a fluid with a finite pressure turns into freely streaming particles.

2.5.1 Thermal spectra of hadrons

In the Cooper and Frye description [42], used here and in most hydrodynamical studies, the decoupling is assumed to take place on an infinitesimally thin decoupling surface σ, which is a three-dimensional hypersurface, usually characterized by a constant temperature $T(x) = T_{\rm dec}$ or constant energy

density[2] $\epsilon(x) = \epsilon_{\rm dec}$.

For matter with a flow velocity $u^\alpha(x)$ the ideal gas distribution is

$$f(x,p) = \frac{g}{(2\pi)^3} \frac{1}{e^{(u^\alpha p_\alpha - \mu)/T} \mp 1} \tag{2.9}$$

in the frame where u^α is measured. The g above counts the spin-degrees of freedom, the minus (plus) sign refers to bosons (fermions) and $\mu(x)$ and $T(x)$ are the chemical potential and temperature.

If $d\sigma^\alpha$ is the surface element of the decoupling surface σ and N^α the particle number four-current, then the total number of particles crossing the decoupling surface σ is

$$N = \int_\sigma N^\alpha d\sigma_\alpha = \int \frac{d^3p}{E} \int_\sigma f(x,p) p^\alpha d\sigma_\alpha. \tag{2.10}$$

Hence, the invariant momentum distribution is [42]

$$E\,\frac{dN}{d^3p} = \int_\sigma f(x,p) p^\alpha d\sigma_\alpha. \tag{2.11}$$

In the case of boost-invariance and cylindrical symmetry, the above relation can be integrated over the space-time rapidity $\eta_{\rm st}$ and the azimuthal angle ϕ. The thermal spectrum of a hadron, with mass m, reduces to the line integral, over $\gamma \in \tau r$-plane,

$$\frac{1}{2\pi p_T}\,\frac{dN}{dy dp_T} = \frac{g}{2\pi^2} \int_\gamma \tau r \sum_{n=1}^{\infty} (\pm 1)^{n+1} e^{n\mu/T} \tag{2.12}$$

$$\times \left[m_T I_0\left(n\gamma_r v_r \frac{p_T}{T}\right) K_1\left(n\gamma_r \frac{m_T}{T}\right) dr - p_T I_1\left(n\gamma_r v_r \frac{p_T}{T}\right) K_0\left(n\gamma_r \frac{m_T}{T}\right) d\tau \right],$$

where the I's and K's are hyperbolic Bessel functions, $T = T_{\rm dec}$, v_r is the radial flow velocity on the decoupling surface and $1/\gamma_r = \sqrt{1 - v_r^2}$ is the corresponding γ-factor [23, 43].

In order to obtain the thermal spectrum of hadron h, the line integration (2.12) is performed for every hadron and hadron resonance h included in the hadronic part of the EoS. This is why the degrees of freedom in the hadron gas need to be known. The chemical potential μ of hadron h is $\mu_h = B_h\mu_B + S_h\mu_S$, where B_h and S_h are the baryon and strangeness numbers of hadron h and $\mu_{B/S}$ the corresponding chemical potentials. Hydrodynamical

[2] These two condition are equal, when $n_B \equiv 0$.

evolution supplies the net-baryon density n_B on the decoupling surface $T = T_{\rm dec}$. The values of the chemical potentials are determined by requiring the local strangeness neutrality and by forming the net-baryon density from free-particle densities, n_h, i.e.

$$0 = \sum_h S_h n_h(T_{\rm dec}, \mu_h) \quad \text{and} \quad n_B = \sum_h B_h n_h(T_{\rm dec}, \mu_h). \tag{2.13}$$

If $n_B \neq 0$, the solution for μ_S is non-trivial, since there are both strange baryons, like lambda's, and strange mesons, like kaons. Although μ_S is small at the collider energies, it leads to a deviation from unity in the strange meson ratios. (see [V] or Table 4.2 below).

2.5.2 Resonance decays and hyperon feed-down

In order to obtain the final observed spectra, resonance decays must be considered since these particles will decay before they reach the detectors. The two and three body decays, whose detailed decay kinematics have been worked out e.g. in [44], have been included with branching ratios (BR) from [45]. Hadrons that do not have strong or electromagnetic decay channels are treated as stable, i.e. all states of

$$\pi,\ \mathrm{K},\ \mathrm{p},\ \mathrm{n},\ \Lambda,\ \Sigma,\ \Xi \text{ and } \Omega$$

and corresponding anti-particles. Σ^0 is the exception since it has an electromagnetic decay channel $\Sigma^0 \to \Lambda + \gamma$.

All hyperons ($\Lambda,\ \Sigma,\ \Xi$ and Ω) have decay chains that end either as proton or neutron, which leads to a contribution from the weak hyperon decays — known as the hyperon feed-down — in the measured proton spectra. The PHENIX and STAR collaborations have published Λ and $\bar{\Lambda}$ spectra measured at RHIC at $\sqrt{s_{NN}} = 130$ GeV [46, 47]. The results support an estimate, presented in [48], which says that ~ 30 % of the measured protons originate from the hyperon decays. The mid-rapidity density dN/dy of protons in the 5 % most central Au+Au collisions at $\sqrt{s_{NN}} = 200$ GeV are 18.4 ± 2.6 and 34.6 ± 6.2, when measured by the PHENIX [49] and STAR [50] collaborations, respectively. The apparent difference in the measured yields comes from the hyperon feed-down contribution, which is extracted from the PHENIX results but included in the STAR results.

2.6 Validity of the boost-invariant approximation

Boost-invariance is an infinite energy limit approximation which is obviously not completely valid, at least in the fragmentation regions, in real heavy ion collisions with finite collision energy. However, it can be argued that an excellent description of the transverse flow is obtained with an assumption of longitudinal scaling flow at the central rapidity region at collider energies [51, 52, 36, V].

In the boost-invariant description, the initial longitudinal flow is of the form of the scaling flow, $v_z = z/t$, and it is assumed to retain this form throughout the evolution. This would only be the case if the initial densities are flat in the space-time rapidity, since in this case there would be no longitudinal pressure gradients to cause deviations in the longitudinal flow velocity.

In [51], the initial energy density resembles a wide Gaussian in the space-time rapidity. The longitudinal flow was initially of the scaling form $v_z = z/t$ but dynamically developed during the evolution. The transverse expansion, however, was neglected and thus the results should supply an upper limit to the modifications in the longitudinal flow, since inclusion of the transverse flow would reduce the lifetime of the system. Differences to the scaling flow were found to be a few percent at the small $|\eta_{st}|$. The transverse flow has been included in [52] where the initial energy density was assumed to be flat, up to $|\eta_{st}| \lesssim 0.5$, and to have a Gaussian tail at the RHIC energy $\sqrt{s_{NN}} = 130$ GeV. Again, at $|\eta_{st}| < 1$ the longitudinal flow deviated from the initially assumed scaling form only by ~ 5 % after a 15 fm/c of hydrodynamical expansion.

When the transverse spectra are calculated using the Cooper and Frye prescription [42] (Eq. (2.12)), the contribution from regions $|\eta_{st}| > 0$ to the mid-rapidity is suppressed by a factor of $\sim e^{-m_T \cosh \eta_{st}/T}$ [23]. This means that the yields at mid-rapidity are not sensitive to the fragmentation regions because only a small fraction of particles in the thermal bath have a large enough energy to end up in the mid-rapidity region over a rapidity gap larger than one.

As deviations, caused by the longitudinal pressure gradients, in the initially assumed scaling flow are small at $|\eta_{st}| \lesssim 1$, from where also the dominant contribution to the transverse spectra of hadrons observed at $y = 0$ comes, boost-invariant hydrodynamics gives an excellent description for both the transverse flow and transverse spectra at central rapidity. However, in these

validity arguments above, the longitudinal flow is assumed to be initially of the scaling form. At the SPS at least, this need not be the case [25].

In the case of exact boost-invariance, where the initial densities are flat everywhere in η_{st}, the final rapidity density dN/dy is also flat. Hence, it has been suggested that in $|y| \lesssim 1$ the formation of a plateau should be seen, which is sometimes called the boost-invariant region. The BRAHMS collaboration [53] has measured the rapidity density of pions and kaons and found them to be well described using Gaussian fits.

The possibility of the formation of a rapidity plateau in the final rapidity density was studied in [36]. With the radial expansion neglected, the authors considered a spectra of massless pions. The longitudinal flow has the scaling form $v_z = z/t$ and the decoupling takes place in an uniform cylinder with a finite extension η_0. In this case, Eq. (2.12) reduces to [36]

$$\frac{dN}{dy} \propto T^3 \left[\tanh(y + \eta_0) - \tanh(y - \eta_0)\right]. \tag{2.14}$$

Thus, the initial densities should be flat over a considerable range before the formation of a plateau in the final measured rapidity density. It remains to be seen if a plateau develops at the LHC energies. Regardless, it should also be noted that the initial densities need not have a flat region at all. For example, based on the pQCD+saturation model [51] or the semi-analytical CGC [37] descriptions for the primary interactions, there is no flat region in the initial densities and hence it most likely does not appear in the final dN/dy either. The boost-invariant description of the transverse flow, however, would still be a justified approximation.

Landau's picture for the initial conditions, where the colliding nuclei are assumed to stop completely, however, can be ruled out. Even at the SPS energies, the net-proton rapidity distribution cannot be even qualitatively reproduced, if full stopping is assumed [26]. Also, the net-proton rapidity density as measured by BRAHMS [54] suggests that the collisions at the RHIC energies are transparent as compared to those at lower energies.

At RHIC, the total collision energy is $E_{\rm tot} = A\sqrt{s_{NN}}$, the transverse area of colliding nuclei $A_T \sim \pi R_A^2$ and the longitudinal thickness $z \sim 2R_A/\gamma \sim 4m_p R_A/\sqrt{s_{NN}}$. The full stopping scenario leads to an initial energy density of the order

$$\epsilon \sim \frac{E_{\rm tot}}{A_T z} \sim \frac{A s_{\rm NN}}{4\pi R_A^3 m_p} \sim \ {\rm TeV/fm^3},$$

in the Au+Au collisions ($A = 197$) at $\sqrt{s_{NN}} = 200$ GeV. For an ideal

gas of gluons and quarks ($N_f = 3$) this corresponds to an (average) initial temperature $T_{\rm ini} \sim 840$ MeV and leads to too large photon emission (see Secs. 2.7 and 4.4.2 and [55]). Also, the shape of the rapidity density of thermal photons is sensitive to the amount of stopping which may provide an experimental test for the separation of different descriptions of the initial longitudinal flow [55].

2.7 Probes of a dense medium

As discussed in Sec. 2.5.1, hadron spectra are determined at the final stage of the evolution and do not directly provide information on the properties of the dense medium. In order to learn about the conditions inside the medium, more penetrating probes are needed.

2.7.1 Thermal photons

It has been suggested that, due to their large mean free path compared to the size of the system [56], photons would be an ideal probe for the hot early stages of the relativistic heavy ion collisions, since they would escape from the collision region without further interactions.

The assumption of thermalization necessitates the emission of thermal photons during the expansion. In principle, the evaluation of the spectrum of thermal photons is straightforward when the emission rate $R \equiv E dN^\gamma/d^4x d^3k$ is known. To obtain the spectrum of emitted thermal photons, the emission rate needs to be integrated over the space-time volume (V_4) where the temperature is larger than the decoupling temperature $T_{\rm dec}$

$$E\frac{dN^\gamma}{d^3k} = \int_{\rm V_4} d^4x \; R\Theta(T - T_{\rm dec}). \tag{2.15}$$

The leading order ($\alpha\alpha_s$) photon emission rate from the thermalized QGP was first obtained in [57, 58], in which two-to-two processes, Compton scattering and $q\bar{q}$-annihilation, were included. This was thought to give the complete leading order result until it was found [59] that bremsstrahlung and pair annihilation, although they naively are $\mathcal{O}(\alpha\alpha_s^2)$, contribute to the leading order due to the enhancement from collinear singularities. The full $\mathcal{O}(\alpha\alpha_s)$ result was obtained in [60] where the leading contributions were isolated and summed to all orders. The authors of [60] also provide a parametrization for the complete leading order rate [61], which is used in the photon emission calculations [II, IV] presented here.

The emission from hadron gas is described with a pseudoscalar-vector Lagrangian which includes mesonic scattering processes $\pi\pi \to \rho\gamma$ and $\pi\rho \to \pi\gamma$ [57]. The $\pi\rho$ channel gets a large contribution from the reaction through the a_1 axial meson $\pi\rho \to a_1 \to \pi\gamma$ [62]. In publications [II, IV] parametrizations provided by the authors of [62, 63] were used. The effects from baryons and heavier mesonic resonances, which are not included in the above rates, are discussed in [64].

Although thermal photons appears to be an ideal probe for the dense medium, a caveat exists. Photons are created in every stage of the collision; there are prompt photons from primary interactions between partons of the incoming nuclei, decay photons of the final state hadrons, especially π^0's and η's, and also photons emitted by high energy quarks when they propagate through the medium (jet-photon conversion). It is known that the decay photons dominate the spectrum and contributions from the other sources, the so called excess photons, are difficult to resolve experimentally. Additionally, isolating the thermal contribution from the excess photon spectrum is an even more cumbersome task.

A discussion on jet-photon conversion [65] is not presented here. However, a recent study [66] indicates that, at RHIC, the contribution from the jet-photon conversion is below both the thermal yield at $k_T \lesssim 2.5$ GeV and the prompt photon yield in larger k_T region. At the LHC, the thermal emission may exceed the contribution from the jet-photon conversion up to the photon transverse momentum $k_T \sim 9$ GeV (see Sec. 6.9 in [67]).

The experimental results for the excess photons and the thermal contribution from the hydrodynamical simulations are presented in Sec. 4.4.

2.7.2 Jet quenching

High energy partons, which are produced in primary interactions, are not expected to thermalize. Instead, they travel through the dense medium losing their energy. The total energy loss has been found to scale as L^2, where L is the extent of the medium [68]. This effect is seen in the suppression of high p_T hadrons, observed in AA-collisions, as compared to the results from proton-proton collisions, scaled by the number of collisions [69, 70, 71, 72, 73, 74]. This phenomenon is known as jet quenching and it has been widely discussed as a probe for the dense medium.

No attempt is made here for a detailed discussion on jet quenching, as the

author has not participated in the calculations regarding it. However, results for charged hadron spectra at the high transverse momentum region are shown for the purpose of comparison with the thermal component. The slopes of the thermal spectra of hadrons are roughly exponential in shape whereas the slopes of the spectra of hadrons, originating from the fragmentation of hard partons, display a powerlaw behaviour in the large transverse momentum region. An intermediate p_T region, where the contribution from jet fragmentation including energy loss becomes comparable with the thermal yield, will be identified.

In [V] the description of the energy loss presented in [75] is utilized to obtain the transverse momentum spectra of hadrons at high p_T. Similar studies combining hydrodynamics and jet quenching are presented by Hirano and Nara [76, 36].

Chapter 3

Initial State from the pQCD+saturation Model

As was observed in Sec. 2.2, the energy and baryon number densities, $\epsilon(\tau_0, r)$ and $n_B(\tau_0, r)$, need to be specified at some finite thermalization time τ_0 for initial conditions of azimuthally-symmetric boost-invariant hydrodynamics. At collider energies [I, III, V], an initial state, obtained from a perturbative QCD (pQCD) calculation with a conjecture of the final state saturation [17], was used.

3.1 Minijet production

In the pQCD+saturation model introduced in Ref. [17], the key quantities in describing primary interactions using perturbation theory are a number-weighted cross section $\sigma\langle N\rangle(p_0, \sqrt{s_{NN}}, A, \Delta y)$ and a transverse energy-weighted cross section $\sigma\langle E_T\rangle(p_0, \sqrt{s_{NN}}, A, \Delta y)$, calculated in a framework of collinear factorization, in a single nucleon-nucleon collision, when the nucleons are bound to a nucleus with mass number A. The quantity $\sigma\langle N\rangle$ is an integrated inclusive cross section for producing a minijet, which has a transverse momentum $p_T \geq p_0$, within a rapidity interval Δy and $p_0 \gg \Lambda_{\rm QCD}$ is the cut-off scale. Dependence on the mass number A exists through the nuclear parton distribution functions $f_{i/A}$. For more details, see Chap. 2 in [V].

The multiplicity of all partons, with $p_T \geq p_0$, produced within the central rapidity interval Δy in an AA-collision is

$$N_{AA}(\mathbf{b}, \sqrt{s_{NN}}, p_0, \Delta y) = T_{AA}(\mathbf{b})\sigma\langle N\rangle(p_0, \sqrt{s_{NN}}, A, \Delta y). \qquad (3.1)$$

Similarly, the transverse energy-weighted minijet cross section $\sigma\langle E_T\rangle$ sup-

plies the transverse energy E_T^{AA} carried by the produced quanta

$$E_T^{AA}(\mathbf{b}, \sqrt{s_{NN}}, p_0, \Delta y) = T_{AA}(\mathbf{b})\sigma\langle E_T\rangle(p_0, \sqrt{s_{NN}}, A, \Delta y). \tag{3.2}$$

In the above relations, $\mathbf{b} = (b_x, b_y)$ is the impact parameter and

$$T_{AA}(\mathbf{b}) = \int d^2s\ T_A(\mathbf{s})T_A(\mathbf{b}-\mathbf{s}) \qquad \text{and} \tag{3.3}$$

$$T_A(\mathbf{s}) = \int_{-\infty}^{\infty} dz\ n_A(\mathbf{s}, z) \tag{3.4}$$

are the nuclear overlap and thickness functions, respectively. The nuclear density n_A is normalized to $\int d^3x\ n_A(\mathbf{x}) = A$. A spherically symmetric Woods-Saxon density

$$n_A^{\rm WS}(\mathbf{x}) = n_A^{\rm WS}(r) = \frac{n_0}{1+\exp[(r-R_A)/d]}, \tag{3.5}$$

is used, where $r = \sqrt{\mathbf{s}^2+z^2}$, nuclear radius $R_A = 1.12A^{1/3} - 0.86A^{-1/3}$, nuclear thickness parameter $d = 0.17$ fm and n_0 is the central density defined by the normalization [77].

The number of produced partons is well defined only in the leading order pQCD since the calculation is not infrared-safe if it is not specified when two nearly collinear partons are to be counted as one. However, the minijet transverse energy calculation can be extended to the next-to-leading order [78, 79] in an infrared-safe manner and this provides a theoretical description for a K-factor. The same K-factor, which has a value $K = 2.3$ (1.6) for RHIC (LHC) [79, I], is also used for multiplicities.

The cross section $\sigma\langle N\rangle$ for all partons can be decomposed to

$$\sigma\langle N\rangle = \sigma\langle N_g\rangle + \sigma\langle N_{\rm q}\rangle + \sigma\langle N_{\bar{\rm q}}\rangle, \tag{3.6}$$

which includes contributions from produced gluons, quarks and anti-quarks, respectively [80, III, V]. The net-baryon number produced within the rapidity interval Δy is simply

$$N_{AA}^{\rm B-\bar{B}} = T_{AA}\frac{1}{3}\left[\sigma\langle N_{\rm q}\rangle - \sigma\langle N_{\bar{\rm q}}\rangle\right] \equiv T_{AA}\sigma\langle N_B\rangle, \tag{3.7}$$

which deviates from zero due to the valence quark scatterings. In order to achieve the initial state for the hydrodynamical evolution, the remaining task is to fix the cut-off momentum p_0 and convert (3.2) and (3.7) to spatial energy and net-baryon number densities (2.7).

3.2 Saturation and initial densities

The idea of a *final* state (of primary interactions) saturation was proposed in [17]. pQCD is known to work at high $p_T \gg 1$ GeV. Perturbative parton production is followed towards smaller values of p_T, where gluons dominate. At some point, the gluon density becomes so large that gluon fusions become important and tame the growth of the gluon number. This procedure is non-perturbative and it is effectively described with the following phenomenological conjecture: a dense minijet system *saturates* when the effective transverse occupation area of perturbatively produced minijets, each of a transverse size π/p_0^2, fill the total transverse area πR_A^2 of the colliding nuclei, i.e.

$$N_{AA}(p_0 = p_{\rm sat}) \times \frac{\pi}{p_{\rm sat}^2} = \pi R_A^2. \tag{3.8}$$

It turns out that the obtained saturation scale has values $p_{\rm sat} \sim 1 \ldots 2$ GeV $\gg \Lambda_{\rm QCD}$ at collider energies and the perturbation theory seems trustworthy in the sense that the K-factors remain stable even down to such small scales [79].

The pQCD calculation of minijet production is formulated in momentum space and a connection to spatial densities needs to be established. At collider energies, $2R_A/\gamma_{\rm cm} \ll 1$ fm so the collision region is considered to be a point in the tz-plane and it is assumed that the rapidity of the minijet y coincides with its space-time rapidity $\eta_{\rm st}$. The saturation scale $p_{\rm sat}$ gives the formation (proper) time $\tau_{\rm form} \sim 1/p_{\rm sat}$ of the minijets. Hence, minijets produced within the rapidity interval Δy are formed along a hyperbola $t = \sqrt{\tau_{\rm form}^2 + z^2}$ with a longitudinal velocity $v_z = z/t$ and occupy a volume $\Delta V(\tau_{\rm form}) A_T \Delta z \approx \pi R_A^2 \tau_{\rm form} \Delta y$. An average density of minijets, after the formation, is

$$\langle n \rangle = \frac{N_{AA}(p_0 = p_{\rm sat})}{\Delta V(\tau_{\rm form})}, \tag{3.9}$$

which has a value $\langle n \rangle \sim 60$ (400) 1/fm^3 at RHIC (LHC) [17]. The average energy- and net-baryon densities $\langle \epsilon \rangle$ and $\langle n_B \rangle$ are obtained similarly by replacing N_{AA} with E_T^{AA} or $N_{AA}^{\rm B-\bar{B}}$ in Eq. (3.9).

Next the bold assumption is made that the produced minijet system thermalizes immediately after it is formed, i.e. the thermalization time $\tau_0 = \tau_{\rm form}$. Some arguments can be given in favour of this assumption. If the temperature T for (gluonic) matter is calculated from $\langle n \rangle \sim T^3$ or $\langle \epsilon \rangle \sim T^4$, the same T for the thermal system should be obtained. This was found to be true within a few percent level in [17] and with respect of the average densi-

ties produced, the (gluonic) minijet system appears thermal. The quantity $\tau_{\rm form} \sim 1/p_{\rm sat}$ is an estimate for overall formation time of (semi-)hard partons. More energetic minijets form earlier and some secondary interactions have already taken place at $\tau = \tau_{\rm form}$. Recent studies on plasma instabilities [81] also suggest a faster thermalization than estimates based on the "bottom-up" scenario [82].

Even if the matter is not fully thermalized at $\tau \sim \tau_{\rm form}$, the pQCD minijet formation suggests that, by that time, a very dense partonic system is formed. In most hydrodynamical studies the thermalization time is taken to be $\tau_0 = 0.6 \ldots 1.0$ fm/c (see e.g. a review [83]). At RHIC, this is a $3-5$ times larger time scale than the formation time of the minijets. Hence, in these studies, secondary collisions, that are required for thermalization, will occur before the hydrodynamical evolution begins. From point of view here, using hydrodynamics with the short thermalization time $\tau_0 = \tau_{\rm form}$ also approximates collisions that lead to the thermalization. The authors of [84] found that the data at the RHIC energy $\sqrt{s_{NN}} = 200$ GeV favour a small initial radial velocity, which can be associated with pre-thermal interactions. This could suggest that the main part of the particle production indeed happens at the time scale $\sim 1/p_{\rm sat}$ and the system also begins the radial expansion at that time, which does not require thermalization. This finite time in between formation and thermalization could be described by using free streaming. However, treating the densest state of the evolution as free streaming, in the authors opinion, does not sound more plausible than using hydrodynamics immediately after the formation. The real situation most likely lies in between these extreme scenarios.

The transverse profiles of the initial densities are extracted by differentiating the overlap function T_{AA} (3.3) with respect to d^2s. The nucleon-nucleon luminosity for a transverse element d^2s is $T_A(\mathbf{b}-\mathbf{s})T_A(\mathbf{s})$ and the differential volume element $dV = \tau_0 dy d^2s$. Thus, the initial densities for the boost-invariant hydrodynamic flow become [I, V]

$$\epsilon(\tau_0 = 1/p_{\rm sat}, \mathbf{s}) = \frac{dE_T}{\tau_0 dy d^2s} = [T_A(\mathbf{s})]^2 \, \sigma \langle E_T \rangle \frac{p_{\rm sat}}{\Delta y} \qquad (3.10)$$

$$n_B(\tau_0 = 1/p_{\rm sat}, \mathbf{s}) = \frac{dN_{AA}^{\rm B-\bar{B}}}{\tau_0 dy d^2s} = [T_A(\mathbf{s})]^2 \, \sigma \langle N_B \rangle \frac{p_{\rm sat}}{\Delta y} \qquad (3.11)$$

for fully central, $\mathbf{b} = \mathbf{0}$, AA-collisions.

Here only (nearly) central collisions, in which the pQCD+saturation description works well, are discussed. Centrality and rapidity dependencies at

the final state saturation model have also been explored [85, 86] but it seems that the pQCD+saturation works when there is only a single dominant scale $p_{\rm sat}$ in the system. For example, as in the case of particle production in central collisions at mid-rapidity. In a peripheral collision the centre of the first nucleus meets the border of the other and the differences in density and thickness may lead to (at least) two separate scales.

3.3 Centrality selection

The assumption of azimuthal symmetry, made in Sec. 2.2, is strictly valid only for fully central collisions. In practice, all experimental results are given in centrality classes which have to be taken into account in order to make a realistic comparison between data and theory.

It is assumed that the centrality can be taken into account by considering fully central collisions of two effective nuclei $A_{\rm eff} < A$, which are determined by the centrality selection. The total inelastic cross section of the AA-collision is written as

$$\sigma_{\rm in}^{\rm AA}(\sqrt{s_{NN}}) = \int d^2b \, [1 - \exp\left(-\sigma_{\rm in}^{\rm pp}(\sqrt{s}) T_{AA}(\mathbf{b})\right)], \tag{3.12}$$

where $\sigma_{\rm in}^{\rm pp}(\sqrt{s})$ is the measured total inelastic cross section in pp-collisions [45]. For RHIC (LHC) some interpolation (extrapolation) must be done to obtain the value of $\sigma_{\rm in}^{\rm pp}(\sqrt{s})$.

An impact parameter range b_r corresponding to a fraction r of the total inelastic cross section is

$$r\sigma_{\rm in}^{\rm AA} \equiv \sigma_{\rm in}^{\rm AA}(b_r) = \int_{|\mathbf{b}|<b_r} d^2b \, [1 - \exp\left(-\sigma_{\rm in}^{\rm pp} T_{AA}(\mathbf{b})\right)] \approx \pi b_r^2. \tag{3.13}$$

The latter approximation is very good when $r \leq 0.1$. The average number of participants in this centrality class can be estimated as

$$\langle N_{\rm part} \rangle_r \approx \frac{1}{\pi b_r^2} \int_{|\mathbf{b}|<b_r} d^2b \; N_{\rm part}(\mathbf{b}), \tag{3.14}$$

where the number of participants in symmetric AA-collisions is computed from

$$N_{\rm part}(\mathbf{b}) = 2 \int d^2s \; T_A(\mathbf{b}-\mathbf{s})[1 - \exp\left(-\sigma_{\rm in}^{\rm pp} T_A(\mathbf{s})\right)]. \tag{3.15}$$

The effective mass number $A_{\rm eff}$ is found by requiring the number of participants in fully central $A_{\rm eff}A_{\rm eff}$-collisions to be equal to $\langle N_{\rm part} \rangle_r$.

3.4 Initial state at the SPS

The pQCD+saturation approach works at the collider energies, but it is not meaningful at lower energies, such as those obtained in the SPS. Minijets represent the hard part of particle production whereas, in the SPS, soft processes are more significant. A reasonable estimate for the applicability of the final state saturation can be obtained from collision geometry.

The saturation momentum $p_{\rm sat}$ scales as [17]

$$p_{\rm sat} = 0.208 A^{0.128} \left(\frac{\sqrt{s_{NN}}}{\rm GeV} \right)^{0.191} \quad {\rm GeV}. \tag{3.16}$$

By using the gamma-factor $\gamma_{\rm cm} \backsimeq \sqrt{s_{NN}}/2m_p \backsimeq 1/2(\sqrt{s_{NN}}/{\rm GeV})$, one obtains an estimate for the transit time of the colliding nuclei $\tau_{\rm tr} \sim 2R_A/\gamma_{\rm cm}$. Naturally, the (assumed) thermalization time $\tau_0 = 1/p_{\rm sat}$ has to be larger than the transit time of the colliding nuclei. In the opposite case, when $\tau_0 < \tau_{\rm tr}$, some primary interactions take place after the assumed thermalization and the formation time cannot be meaningfully estimated from the saturation momentum. Using $R_A \sim 1.12 A^{1/3}$ fm, the condition $\tau_0 > \tau_{\rm tr}$ is fulfilled when [17]

$$\frac{\sqrt{s_{NN}}}{\rm GeV} \gtrsim 6.8 A^{0.57}. \tag{3.17}$$

For RHIC energies $\tau_0 \sim \tau_{\rm tr}$, while at the SPS $\tau_0 \ll \tau_{\rm tr} \sim 1$ fm/c in contradiction with the longitudinal geometry. At the LHC $\tau_0 \gg \tau_{\rm tr}$ and the collision region in the tz-plane is much closer to a point as compared to RHIC. Thus, the pQCD+saturation model could perform even better at the LHC energies.

At the SPS energies [II, IV], the initial state for the boost-invariant hydrodynamics have been taken from [87]. The initial energy density at the transverse plane is assumed to be proportional to the number of wounded nucleons. The thermalization time and normalizations of the initial densities are free parameters. The authors of [87] chose $\tau_0 = 0.8$ fm/c and fixed the normalizations according to experimentally observed multiplicity in central collisions.

Initial states used at the SPS energy are described in more detail in Sec. 4.4 where thermal photons are considered. This is because the electromagnetic probes are sensitive to details of the initial state.

Chapter 4

Results

4.1 Initial conditions in collider energies

Chap. 3 outlined how the initial state is constructed at the collider energies. Results from the pQCD+saturation approach are collected to Table 4.1. The

$\sqrt{s}/A$ [GeV]	130	200			5500
Centrality	5 %	5 %	10 %	15 %	5 %
$A_{\rm eff}$	181	181	166	153	193
$T_{A_{\rm eff}A_{\rm eff}}(0)$ [1/mb]	26.1	26.1	23.1	20.6	28.5
$N_{\rm part}$	346	347	318	293	376
$p_{\rm sat}$ [GeV]	1.06	1.15	1.14	1.12	2.01
τ_0 [fm/c]	0.19	0.17	0.17	0.18	0.10
$\sigma\langle E_T\rangle$ [mbGeV]	67.0	85.9	88.3	90.7	479
$\sigma\langle N^g\rangle$ [mb]	37.3	44.6	46.4	48.2	140
$\sum_q \sigma\langle N^q\rangle$ [mb]	4.66	4.58	4.75	4.92	6.66
$\sum_q \sigma\langle N^{\bar{q}}\rangle$ [mb]	2.76	2.98	3.10	3.21	6.34
$\sigma\langle N\rangle$ [mb]	44.7	52.2	54.3	56.3	153
$\sigma\langle N^{B-\bar{B}}\rangle$ [mb]	0.635	0.536	0.553	0.570	0.109

Table 4.1: The pQCD quantities computed [V] with $p_0 = p_{\rm sat}$ in the central $A_{\rm eff}$+$A_{\rm eff}$ collisions at RHIC and LHC corresponding to various experimental centrality selections. The saturation scales, corresponding formation times, number of participants and the overlap function at $\mathbf{b} = \mathbf{0}$ are shown.

pQCD+saturation approach is a closed phenomenological framework to describe the primary production in mid-rapidity. Within the assumptions presented in Chap. 3, initial densities — including their normalizations — are fully determined when the mass number of the colliding nuclei, CMS energy and experimental centrality selection are given.

As can be seen from the results in Table 4.1, the formation time of the dense minijet system is $\tau_0 = 0.1 \ldots 0.2$ fm/c in collider energies at RHIC and LHC. The average initial densities can be obtained using Eq. (3.9). For example, when the average initial parton and energy densities in the 5 % most central Au+Au collision at $\sqrt{s_{NN}} = 200$ GeV are

$$\langle n \rangle \approx 67 \ 1/\mathrm{fm}^3 \quad \text{and} \quad \langle \epsilon \rangle \approx 110 \ \mathrm{GeV}/\mathrm{fm}^3 \tag{4.1}$$

at $\tau_0 = 1/p_{\mathrm{sat}} = 0.17$ fm/c. Similarly, the total net-baryon number, in central rapidity $y = 0$ at RHIC, $dN^{B-\bar{B}}/dy \simeq N_{AA}^{B-\bar{B}}/\Delta y = T_{A_{\mathrm{eff}}A_{\mathrm{eff}}}\sigma\langle N_B \rangle \approx 14.0$ is a prediction of the pQCD+saturation approach.

However, to compare the net-baryon number in central rapidity with experimental results, the hydrodynamical evolution must be gone through in order to obtain the chemical composition of the net-baryon number. This is because the pQCD + saturation approach only counts the difference of produced quarks and anti-quarks. A hydrodynamical simulation [V], using $T_{\mathrm{dec}} = 150$ MeV, gives the final state multiplicities $\mathrm{p} - \bar{\mathrm{p}} \approx \mathrm{n} - \bar{\mathrm{n}} \approx 5.5$, $\Lambda - \bar{\Lambda} \approx 2.3$ and smaller contributions from heavier hyperons included in the EoS. The obtained net-proton rapidity density agrees with the experimental result $\mathrm{p} - \bar{\mathrm{p}} = 6.4 \pm 0.4(\mathrm{stat}) \pm 1.0(\mathrm{sys})$ measured by the BRAHMS collaboration [54].

The initial energy and net-baryon density profiles, from which the hydrodynamical evolution begins, are given by Eq. (3.10). The resulting energy densities in 5 % most central Au+Au collisions at RHIC and the Pb-Pb collisions at the LHC are shown in Fig. 4.1.

It should be noted, that $\sigma\langle N_g \rangle / \sigma\langle N \rangle \sim 0.85$ (0.91) at RHIC (LHC), which means that the produced minijet system is roughly 90 % gluonic after the formation. In fully thermalized ideal plasma, the contribution of gluons to the total thermal density $n_{\mathrm{ther}} = \left(g_B + \frac{3}{4}g_F\right)\frac{\zeta(3)}{\pi^2}T^3$ would be $16/(16 + 9N_f) \approx 0.37$ for $N_f = 3$. The expected gluon dominance in the pQCD+saturation description of the primary production thus indicates that even if the produced particles may be close to the kinetic equilibrium, they will be far from the chemical equilibrium.

Since it is assumed that the matter is fully thermalized at the formation ($\tau_{\mathrm{ther}} = \tau_{\mathrm{form}}$), the particle densities follow the thermal densities throughout hydrodynamical evolution. In a more realistic calculation [67] the deviation from the chemical equilibrium has been described, by use of the multiplica-

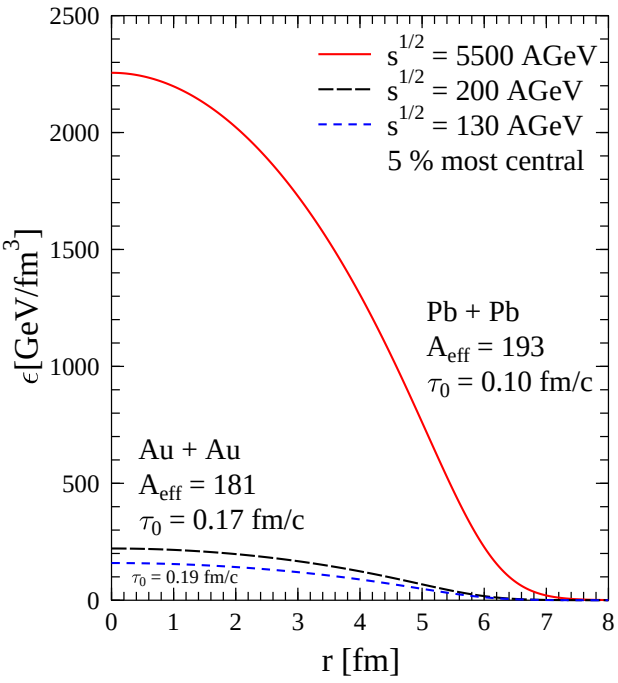

Figure 4.1: Transverse profile of the initial energy density in an average $A_{\rm eff}$+$A_{\rm eff}$ collision in the 5 % most central collisions at the LHC (solid line) and RHIC (dashed lines). Formation times and effective nuclei are indicated, see Table 4.1.

tive fugacity factors in the QGP part of the EoS. The evolution of fugacities is determined by solving the rate equations [88, 89] together with the hydrodynamical evolution equations.

The hydrodynamical evolution is driven by the pressure. Since, for a relativistic ideal gas of massless particles $P = \epsilon/3$, the out-of-chemical equilibrium does not change the evolution in the plasma phase[1]. It also has been found [67] that the lifetime of the plasma phase is long enough for the system to nearly equilibrate before entering the hadronic phase of the evolution. (However, equilibrium is approached more slowly with different initial conditions for fugacities [88, 89].)

As was discussed in Sec. 2.5, hadron spectra are determined from condi-

[1] In [67] the bag constant is a function of fugacities causing minor changes to the evolution near the phase transition region.

tions at the decoupling. Since the evolution of the transverse flow does not change significantly and the chemical equilibrium is reached before the hadronization, the chemical non-equilibrium is not expected to affect the results presented in [I, III, V] appreciably.

In the non-equilibrium case, there are less degrees of freedom in the plasma phase as compared with the equilibrium case. As a result, at a given energy density, the parton densities are smaller and the temperatures higher in the non-equilibrium plasma, although the pressure remains the same. These effects have important consequences for the photon emission studied in [IV]. This is discussed further in Sec. 4.4.

4.2 Global observables

In [I], global observables (i.e. integrated quantities such as multiplicities and transverse energies) were studied in the case where also a radial expansion and a realistic hadron gas were included to improve the estimates presented in [17], in which only the longitudinal expansion was considered.

The main results in [I] are summarized in Figs. 4.2 and 4.3, which show the total multiplicity dN/dy and transverse energy dE_T/dy at $y = 0$ as a function of the CMS energy $\sqrt{s_{NN}}$. The open triangles correspond to results for fully central Au+Au collisions and the open squares for Pb+Pb collisions. The filled symbols represent the 6 % most central collisions. Results without the transverse expansion [17], presented as lines in Figs. 4.2 and 4.3, are calculated for fully central collisions and should be compared to the open symbols.

The total (charged) multiplicity can be estimated using the pQCD+saturation model. This is done by assuming the entropy conservation and entropy per particle ratio $S/N \sim 4$, and that together, they relate the final multiplicity of hadrons to the number of partons N_f produced to the mid-rapidity interval Δy in the primary interactions as $dN/dy \sim 1.03 N_f$ [17].

As seen from results in Fig. 4.2, the total multiplicity does not change appreciably when the transverse expansion is included on top of the longitudinal expansion. With or without transverse expansion, the entropy in the rapidity unit is conserved in the hydrodynamical expansion, except for a small numerical diffusion. However, at RHIC, the results with the transverse expansion tend to have larger values compared to those found in [17]. As discussed in [I], there are compensating effects which explain these small

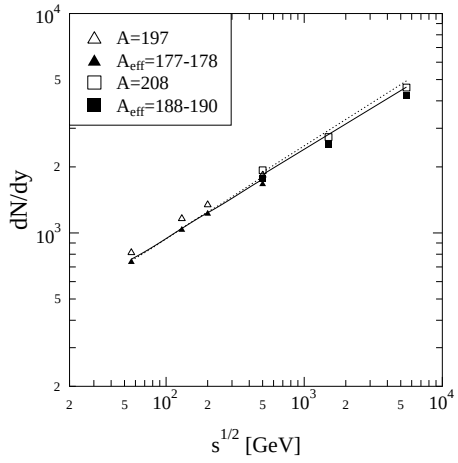

Figure 4.2: Total particle multiplicity dN/dy at $y = 0$ for $\sqrt{s_{NN}} = 56$, 130, 200, 500, 1500 and 5500 GeV. The open triangles are for central Au+Au collisions and the open squares for central Pb+Pb collisions. The filled symbols correspond to the 6 % most central collisions. The lines show the results obtained in [17].

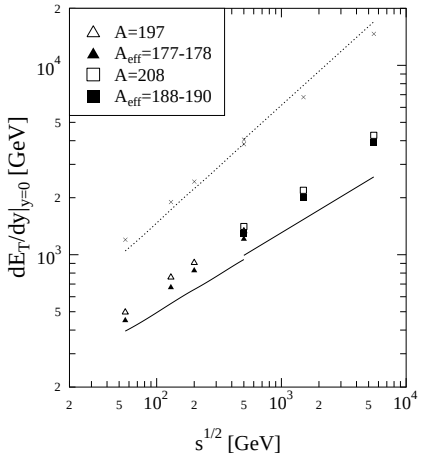

Figure 4.3: As in Fig. 4.2 but for the total transverse energy dE_T/dy. The dotted line show the initial transverse energy and the solid line a prediction for final transverse energy [17]. For details, see the text.

deviations. The most important ones are: the increase of the initial entropy density $s \sim g^{1/4}\epsilon^{3/4}$ when the contribution from (anti)quarks is included with that of gluons in the effective degrees of freedom g. Yet, the ratio s/n increases when a more realistic hadron resonance gas is considered at the final state, instead of the massive pion gas.

The transverse energy is reduced by the pdV work done in the longitudinal expansion of the fluid. The solid (dotted) lines in Fig. 4.3 show predictions for the final (initial) transverse energy presented in [17]. The initial values correspond to the transverse energy of produced partons at saturation. The final transverse energy is obtained by considering longitudinal Bjorken expansion in the case of an ideal gas equation of state, which leads to

$$E_T(\text{final}) = (T_f/T_0)E_T(\text{initial}), \tag{4.2}$$

where T_f and T_0 are the final and initial temperatures. The final temperature was chosen to be $T_f = 180$ MeV since the scaling relation above is valid

for the ideal gas EoS, i.e. only in the plasma phase. Also, the transverse timescale, $\tau_T \sim \sqrt{3}R_A \sim 11$ fm/c for $A = 197 \ldots 208$, provides a rough estimate for a time by which the rarefaction wave has penetrated from the edge of the system to the center and the radial expansion also becomes important [22]. At RHIC, the longitudinal expansion alone cools the system down to the phase transition temperature within $\tau_c \sim 6$ fm/c $< \tau_T$, but at the LHC $\tau_c \sim 20$ fm/c $> \tau_T$ [17, V]. Thus the transverse expansion was predicted to become important already in the plasma phase at the LHC [17]. This was verified in [V], where the lifetime of the plasma phase, in the center of the fireball $r = 0$, was found to be $\tau_c(r = 0) \approx 5.5$ fm/c at RHIC and 7.5 fm/c at the LHC. (See Figs. 4.5 and 4.6.)

The results for dE_T/dy with transverse expansion [I], the squares and triangles in the Fig. 4.3, lie in-between the initial and final values obtained with the longitudinal expansion only. With the transverse expansion, the reduction in the transverse energy is less, as would be expected, due to the build up of the transverse flow. However, the transverse flow cannot fully compensate for the energy transfer to the longitudinal motion and the reduction from the initial values is still considerable: a factor of ~ 2.7 at RHIC and ~ 3.6 at the LHC.

The results for the global observables [V] have been collected in Table 4.2, which shows the multiplicities and transverse energies in the 5 % most central Au+Au collisions at $\sqrt{s_{NN}} = 130$ and 200 GeV. The results are given with two decoupling temperatures, $T_{\rm dec} = 120$ and 150 MeV, both with and without the feed-down contributions. The results with the feed-down are presented in parentheses. As noted in [I], the choice of the decoupling temperature (and the feed-down contributions) causes less than 10 % effects in the total multiplicities and transverse energies. However, both decoupling temperature and feed-down contributions are important when the (anti)proton or lambda yields are considered.

Table 4.3 presents experimental results for the dN/dy of π^+, $\mathrm{K}^\pm$ and (anti)-protons measured by PHENIX [49] and STAR [50] collaborations in the 5 % most central Au+Au collisions at $\sqrt{s_{NN}} = 200$ GeV. Experimental results for pions and kaons agree with calculated values within the experimental uncertainties. The PHENIX collaboration have extracted feed-down contributions from their data while these are included in the STAR collaborations data. As can be seen from the measured yields, the feed-down contributions are considerable in the (anti)proton data. However, based on the pion and kaon yields, which are fairly insensitive to feed-down, it seems that STAR

$\sqrt{s_{NN}}$ [GeV]	130		200	
$T_{\rm dec}$ [MeV]	120	150	120	150
dN/dy(tot)	1012 (1023)	1098 (1134)	1248 (1261)	1315 (1358)
$dN/d\eta$(tot)	896 (904)	927 (954)	1111 (1122)	1120 (1153)
dN/dy(char)	625 (634)	662 (690)	771 (781)	793 (826)
$dN/d\eta$(char)	557 (564)	566 (587)	691 (699)	683 (708)
dE_T/dy(tot) [GeV]	655 (655)	692 (691)	838 (838)	857 (856)
$dE_T/d\eta$(tot) [GeV]	588 (589)	578 (579)	760 (760)	726 (727)
dN^{π^+}/dy	265 (267)	259 (269)	327 (330)	310 (323)
dN^{π^0}/dy	291 (295)	287 (300)	359 (364)	344 (360)
dN^{π^-}/dy	265 (270)	259 (272)	327 (332)	310 (325)
$dN^{\rm K^+}/dy$	40.7 (40.8)	51.2 (51.2)	49.9 (49.9)	60.7 (60.8)
$dN^{\rm K^-}/dy$	38.2 (38.2)	48.2 (48.3)	47.7 (47.7)	58.4 (58.5)
$dN^{\rm p}/dy$	9.8 (13.5)	20.2 (29.7)	10.2 (14.2)	22.5 (33.2)
$dN^{\bar{\rm p}}/dy$	3.3 (4.7)	13.1 (19.8)	4.8 (6.8)	17.0 (25.6)
dN^{Λ}/dy	4.0 (5.0)	9.7 (12.6)	4.2 (5.3)	10.9 (14.3)
$dN^{\bar{\Lambda}}/dy$	1.4 (1.8)	6.8 (9.0)	2.1 (2.6)	8.7 (11.4)
$\bar{\rm p}/{\rm p}$	0.34 (0.35)	0.65 (0.67)	0.47 (0.48)	0.76 (0.77)
$\bar{\Lambda}/\Lambda$	0.36 (0.37)	0.70 (0.71)	0.49 (0.50)	0.79 (0.80)
$dN_{B-\bar{B}}/dy$	16.6		14.0	

Table 4.2: Multiplicities and total transverse energies with and without feed-down contributions for the 5 % most central Au+Au collision with $\sqrt{s_{NN}} = 130$ and 200 GeV. Result with feed-down are presented in parentheses. Also the prediction for the net-baryon number is shown.

obtains slightly larger yields than PHENIX. Also, the multiplicity of protons at mid-rapidity $dN^{\rm p}/dy = 34.7 \pm 6.2$, obtained by STAR [50], agrees with BRAHMS result [54] $dN^{\rm p}/dy = 26.6 \pm 0.6$(stat)$\pm 1.6$(sys) within the given errors. However, the mean value given by STAR is clearly higher. When the feed-down contributions are extracted from the data, BRAHMS obtains $dN^{\rm p}/dy = 17.5 \pm 1.2$(stat)$\pm 3.0$(sys) in accordance with PHENIX result.

The results [V] in Table 4.2, obtained using $T_{\rm dec} = 150$ MeV and including feed-down, agree with STAR results. However, it should be noted that the kaon multiplicity has been marginally exceeded. A comparison to the PHENIX data, where the feed-down is extracted, leads to a similar conclusions. However, here the (anti)proton multiplicities were also overshot.

It is important to note that, in both cases the calculated (anti)proton yields

dN/dy	π^+	K^+	K^-	p	$\bar{p}$
PHENIX	286.4 ± 24.2	48.9 ± 6.3	45.7 ± 5.2	18.4 ± 2.6	13.5 ± 1.8
STAR	322 ± 32	51.3 ± 7.7	49.5 ± 7.4	34.7 ± 6.2	26.7 ± 4.0

Table 4.3: Experimental results for dN/dy in the 5 % most central Au+Au collisions with $\sqrt{s_{NN}} = 200$ GeV from the PHENIX [49] and STAR [50] collaborations. The PHENIX results are corrected for the feed-down contribution but the STAR results are not.

would be clearly less than the experimental value if $T_{\rm dec} = 120$ MeV was chosen, as was done in [I]. The total multiplicities and transverse energies are insensitive to the choice of $T_{\rm dec}$ since the main contribution to both of them comes from the low-p_T pions, for which the transverse spectra turn out to be rather independent of $T_{\rm dec}$ (see Sec. 4.3).

The decoupling temperature is a free parameter in the pQCD+saturation+ hydrodynamics framework considered here. The results for multiplicities at RHIC energy $\sqrt{s_{NN}} = 200$ GeV could be tuned by choosing $T_{\rm dec} = 140$ MeV, in which case $dN^{\rm p}/dy = 18.3$ (26.6) and $dN^{\bar{\rm p}}/dy = 12.9$ (19.0) are obtained without (with) the feed-down contributions. These results are in perfect agreement with the PHENIX and BRAHMS results but under the yields obtained by STAR.

Particle ratios, especially those involving (anti)protons, depend on the decoupling temperature. Table 4.4 shows the results found for various particle ratios in the 5 % most central Au+Au collisions at $\sqrt{s_{NN}} = 200$ GeV together with the PHENIX data [49].

As shown in Table 4.4, $\pi^-/\pi^+ > 1$. In this calculation, the multiplicity of negative pions is larger than that of positive ones as a result of the following decays of hyperons (and their excited states) [45]: $\Lambda \to {\rm p} + \pi^-$ (BR ≈ 64 %) results in more negative pions because $\Lambda - \bar{\Lambda} > 0$ when $n_B > 0$. The situation is similar for the negative cascade $\Xi^- \to \Lambda + \pi^-$ (BR ≈ 100 %). For sigmas, one finds $\Sigma^- \to {\rm n} + \pi^-$ with BR ≈ 100 % while $\Sigma^+ \to {\rm n} + \pi^+$ "only" with BR ≈ 48 %, since there is another, also Cabibbo-suppressed, decay channel $\Sigma^+ \to {\rm p} + \pi^0$ with BR ≈ 52 %. Thus, these decays produce more negative pions when $\Sigma - \bar{\Sigma} > 0$. The decays of the Ω^- mainly feed Λ's and Ξ's. As seen from Table 4.2, one would obtain $\pi^-/\pi^+ = 1$ when the hyperon feed-down is not considered. These results for π^-/π^+ are consistent with the PHENIX data [49] within the given systematic errors.

$T_{\rm dec}$ [MeV]	120	140	150	PHENIX (stat+sys)
π^-/π^+	1.007	1.007	1.007	$0.984 \pm 0.004 \pm 0.057$
$\mathrm{K}^-/\mathrm{K}^+$	0.958	0.962	0.963	$0.933 \pm 0.007 \pm 0.054$
$\bar{\mathrm{p}}/\mathrm{p}$	0.488	0.716	0.776	$0.731 \pm 0.011 \pm 0.062$
K^+/π^+	0.151	0.182	0.188	$0.171 \pm 0.001 \pm 0.010$
K^-/π^-	0.144	0.174	0.180	$0.162 \pm 0.001 \pm 0.010$
p/π^+	0.043	0.080	0.102	$0.064 \pm 0.001 \pm 0.003$
$\bar{\mathrm{p}}/\pi^-$	0.021	0.057	0.079	$0.047 \pm 0.001 \pm 0.002$

Table 4.4: Experimental results for particle ratios in the 5 % most central Au+Au collisions at $\sqrt{s_{NN}} = 200$ GeV from PHENIX [49]. The hydrodynamical results using $T_{\rm dec} = 120$, 140 and 150 MeV are presented with feed-down contribution from hyperons.

In the results $\mathrm{K}^-/\mathrm{K}^+ < 1$ due to the required local strangeness neutrality (2.13): when net-baryon number $n_B > 0$, the net-strangeness from hyperons is balanced — in particular — by positive kaons. Again, the results agree with the experimental data within the systematic errors.

The result for $\bar{\mathrm{p}}/\mathrm{p}$ agrees with the PHENIX result for $T_{\rm dec} = 140 \ldots 150$ MeV but is clearly less than the experimental value if $T_{\rm dec} = 120$ MeV is chosen. This can be understood with the following rough estimate: regardless of the decoupling temperature $\mathrm{p}(1 - \frac{\bar{\mathrm{p}}}{\mathrm{p}}) = \mathrm{p} - \bar{\mathrm{p}} \sim \frac{1}{3}(B - \bar{B}) \equiv \frac{1}{3}\Delta B$ which leads to

$$\frac{\bar{\mathrm{p}}}{\mathrm{p}} \sim 1 - \frac{\Delta B}{3p}. \tag{4.3}$$

The above ΔB is determined by the pQCD+saturation model and is conserved during the evolution while the proton multiplicity p depends on the $T_{\rm dec}$. It should also be noted that $\bar{\mathrm{p}}/\mathrm{p}$, and hence $\mathrm{K}^-/\mathrm{K}^+$, differ from unity in this calculation due to the non-zero $\sigma\langle N_B \rangle$ (see Table 4.1), which essentially measures the number of valence quarks scattered to the mid-rapidity.

The K/π, and in particular p/π ratios, are not as well reproduced but, nevertheless, both multiplicities and particle ratios are surprisingly close to the experimental results with a single and high decoupling temperature $T_{\rm dec} \sim 150$ MeV.

4.3 Hadron spectra

4.3.1 Results at RHIC

The results for the hadron spectra were compared with the data in [43] when spectra for negatively charged hadrons at RHIC energy $\sqrt{s_{NN}} = 130$ GeV, measured by the STAR collaboration [90], were first published. This first data already indicated, that the final hadron spectra obtained are too shallow if $T_{\rm dec} = 120$ MeV is used, which was chosen based on the hydrodynamical studies at the SPS (see e.g. [24]). The spectra of identified hadrons, measured by the PHENIX collaboration [48], also showed that, if $T_{\rm dec} = 120$ MeV was chosen, the data for the transverse spectra of pions is clearly overshot and furthermore too few (anti)protons were obtained.

The spectra of identified hadrons measured by the PHENIX collaboration [48] are shown in Fig. 4.4. The results from [III] are shown for three different decoupling temperatures $T_{\rm dec} = 120$, 150 and 160 MeV. The spectra of nega-

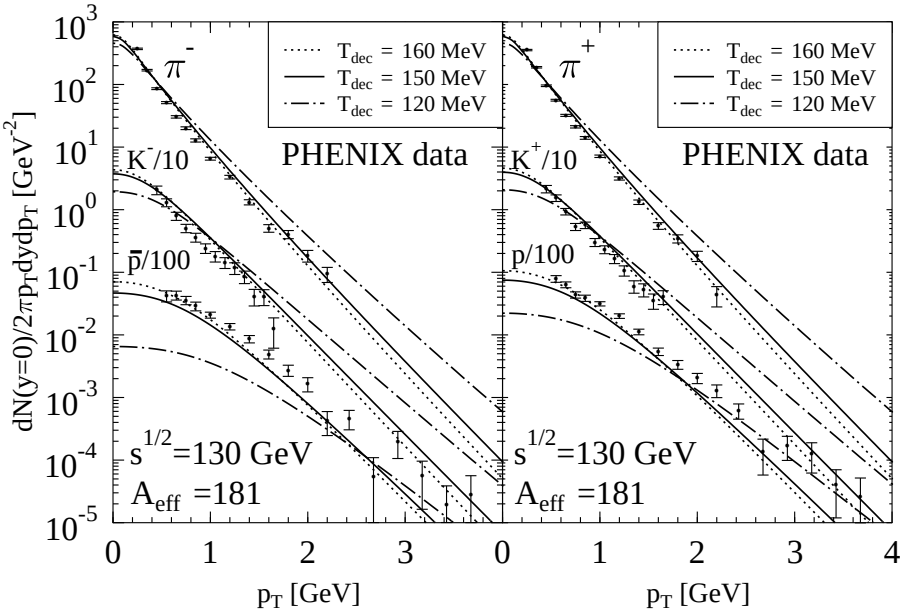

Figure 4.4: Transverse momentum spectra of identified hadrons in the 5 % most central Au+Au collisions at $\sqrt{s_{NN}} = 130$ GeV. The data is from the PHENIX collaboration [48] and the curves are the results from [III] using $T_{\rm dec} = 120$, 150 and 160 MeV.

tive (positive) hadrons are presented in the left (right) panel. The PHENIX data includes ~ 30 % feed-down contributions from the hyperons but the hydrodynamical results without the feed-down are presented in Fig. 4.4.

The hyperon feed-down is mainly seen as an enhancement in the low-p_T region of the transverse momentum spectra of (anti)protons. Hydrodynamical results with feed-down contributions are presented in Fig. 10 in Ref. [V].

As depicted in Fig. 4.4, the overall agreement with the PHENIX data [48] is rather good for both shapes and normalizations of pion, kaon and proton spectra with a single decoupling temperature $T_{\rm dec} = 150 \ldots 160$ MeV. It is (perhaps) a little surprising that the pion spectra also become steeper when the decoupling temperature is raised from 120 to 150 MeV. The Cooper and Frye prescription (Eq. (2.12)) shows that the contributions to the $p_T \gtrsim 1$ GeV range of the transverse spectra come from the regions of the decoupling surface where $v_r \gtrsim 0.5$. Under these conditions, the slopes of the spectra behave approximately as $\sim \exp\left(-p_T/T_{\rm dec}\sqrt{\frac{1+v_r}{1-v_r}}\right) \equiv \exp(-p_T/T_{\rm eff})$. If the radial flow velocity v_r grows fast enough in the evolution, the $T_{\rm eff}$ also grows and the final spectra are more shallow with smaller decoupling temperatures.

Now the slopes of the spectra of identified hadrons will be examined in more detail. Figs. 4.5 and 4.6 show the phase boundaries and two different de-

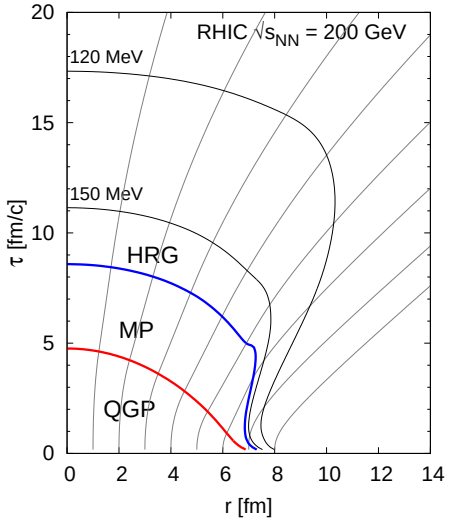

Figure 4.5: The phase boundaries and the two decoupling curves studied, $T_{\rm dec} = 150$ and 120 MeV, with selected flowlines in the plane of proper time τ and transverse variable r in the 5% most central Au+Au collisions at $\sqrt{s_{NN}} = 200$ GeV.

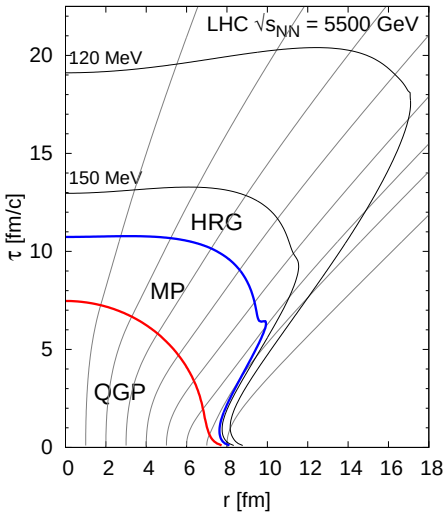

Figure 4.6: As in Fig. 4.5 but for the 5 % most central Pb+Pb collisions at $\sqrt{s_{NN}} = 5500$ GeV.

coupling curves, for $T_{\rm dec} = 150$ and 120 MeV, and a selection of flowlines of the 5 % most central Au+Au and Pb+Pb collisions at $\sqrt{s_{NN}} = 200$ GeV and $\sqrt{s_{NN}} = 5500$ GeV, respectively [V]. As discussed in [III], a flowline starting from $r = 5$ fm at τ_0 crosses the decoupling surface at the region which dominates the tail of the final (thermal) spectra, where the slope of the spectra can be analyzed by studying $T_{\rm eff}$. In [III] the development of $T_{\rm eff}$ as a function of the falling temperature was studied as determined along the flowline in question.

While the actual space-time evolution is markedly different with different equations of state, some general observations can be made with regards to the development of the flow. The effective temperature $T_{\rm eff}$ was shown [III] to grow — along a flowline — if there is a first order phase transition in the EoS but also in the case where a rich hadron gas EoS is considered without the phase transition. However, in the case of a massive pion gas EoS without a phase transition, the $T_{\rm eff}$ and slopes of the final thermal pion spectra were almost independent on the choice of $T_{\rm dec}$. These observations can be explained as follows [III, V]: In the case of a massive pion gas, without phase transition, the EoS is hard which leads to fast growth of flow. At the same time, the temperature drops rapidly and, as a result, $T_{\rm eff}$ remains nearly constant. When a rich hadron gas, without phase transition, is considered, the EoS is soft but the lifetime of the system grows as the energy release from the heavy resonance states slows down the decrease of temperature. With a longer lifetime, growth of the flow overcomes the decrease of the temperature, leading to a growth of $T_{\rm eff}$. The inclusion of the first order phase transition to the EoS was shown to lead to a similar increase of the slopes of the thermal spectra. The strength of the phase transition can be measured using the latent heat between the two phases. A larger latent heat leads to a stronger deflagration from the mixed phase to the hadron gas, which results in the growth of $T_{\rm eff}$. Also, as long as a first order phase transition is included, the slopes of the final spectra are not very sensitive to the number of resonance states that are included in the hadron gas. Reducing the number of heavy hadrons and resonances makes the hadron gas part of the EoS harder and the deflagration stronger (i.e. the latent heat larger), but the resulting stronger growth of flow is compensated by a faster drop of temperature and a shorter system lifetime. Correspondingly, increasing the number of hadronic states reduces the latent heat and makes the hadronic part of the EoS softer, leading to slower growth of flow but, since the temperature drops more slowly, the flow has time to build up.

The discussion now turns to the results for central Au+Au collisions at

$\sqrt{s_{NN}} = 200$ GeV. Fig. 4.7 shows the transverse momentum spectra of

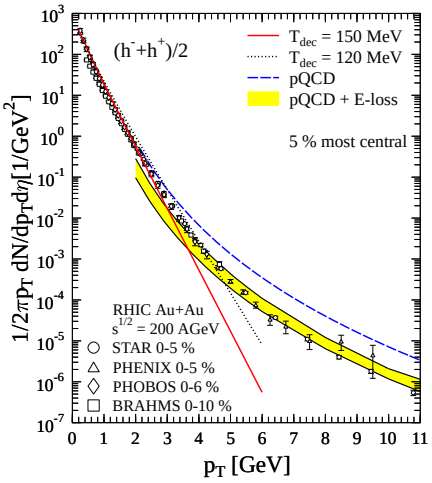

Figure 4.7: Transverse momentum spectra of charged particles at $\eta = 0$ in the 5 % most central Au+Au collisions at $\sqrt{s_{NN}} = 200$ GeV. The hydrodynamic results are shown for $T_{\rm dec} = 150$ MeV (solid line) and $T_{\rm dec} = 120$ MeV (dotted line). The data shown was taken by STAR [72], PHENIX [71], PHOBOS [73] and BRAHMS [74] in the centrality classes indicated.

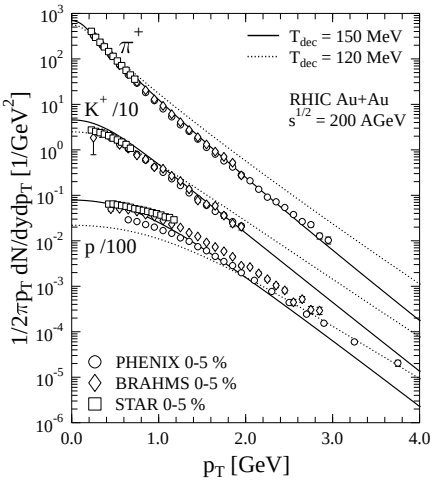

Figure 4.8: Transverse momentum spectra of positive pions, positive kaons and protons at $y = 0$ in the 5 % most central Au+Au collisions at $\sqrt{s_{NN}} = 200$ GeV. The solid lines show the hydrodynamic results with $T_{\rm dec} = 150$ MeV and the dotted lines the results with $T_{\rm dec} = 120$ MeV. The PHENIX data [49] and the BRAHMS data [53, 92] are shown with statistical errors and the STAR data [50] by the given total error bars. The hydrodynamic calculation and the PHENIX data are without the hyperon feed-down contributions but the STAR and BRAHMS data include the feed-down.

charged hadrons in the central Au+Au collisions at $\sqrt{s_{NN}} = 200$ GeV as measured by the STAR [72], PHENIX [71], PHOBOS [73] and BRAHMS [74] collaborations. The hydrodynamical results presented in [V] with $T_{\rm dec} = 150$ (solid line) and $T_{\rm dec} = 120$ MeV (dotted line) are shown. Contributions from the hyperon feed-down are included in the hydrodynamical spectra. Fig. 4.7 clearly shows that the bulk properties of the expanding fireball are well described when the initial state of the hydrodynamics is taken from the pQCD+saturation model [17]. Hydrodynamics can describe the spectra of charged particles up to $p_T \lesssim 2-3$ GeV, which is the same applicability

region for a hydrodynamical description, as suggested by studies on elliptic flow, see e.g. [32].

For comparison, the result from jet fragmentation[2] without and with energy loss are considered for spectra of charged particles in Fig. 4.7 (and in Fig. 4.13 below). The jet fragmentation results, without energy losses, are calculated using the leading order pQCD, nuclear parton distribution functions, fragmentation functions and the energy dependent K-factor, which is determined from the experimental data for pp-collisions [91, V]. These results provide baseline pQCD spectra in AA-collisions. The energy loss is incorporated to these baseline spectra in terms of quenching weights, which are generalized probabilities for a parton to lose an amount ΔE of its original energy [75, V]. As the quenching weights are computed using the eikonal approximation, the energy loss of a jet can, in principle, be arbitrarily large. Since the parton energies are finite in real collisions, it may happen that probabilities to lose $0 \leq \Delta E \leq E_{\rm jet}$ of energy are not properly normalized. This may lead to too large a suppression and thus the calculation gives the lower limit for the results with energy loss. The upper limit is obtained by reweighting the quenching weights such that the probability conservation is enforced. For more details, see [75].

In Fig. 4.7 the dashed line represent the baseline pQCD calculation for jet fragmentation in the case where no energy losses are taken into account [91, V]. The yellow band, between the upper and lower limits described above, shows the results with energy loss. It is observed that at high-p_T, the measured spectra are clearly suppressed as compared to the baseline pQCD spectrum without energy loss (dashed line) [91, V] while the results which include the energy loss [75, V] (yellow band) nicely describe[3] the region $p_T \gtrsim 3.5$ GeV. In the intermediate p_T region neither hydrodynamics nor the pQCD+energy loss calculation is sufficient to describe the data but both are needed.

Fig. 4.8 shows the spectra of positive pions, kaons and protons in the 5 % most central Au+Au collisions at $\sqrt{s_{NN}} = 200$ GeV. The data was taken by the PHENIX [49], STAR [50] and BRAHMS [53, 92] collaborations. The feed-down contributions are extracted from the PHENIX data but the STAR and BRAHMS data contain the feed-down contributions. All the experi-

[2]Studies of jet fragmentation and jet energy losses are performed by other authors (KJE and HH) of [V].

[3]To a certain extent by construction, since the value of the transport coefficient, that characterizes the energy loss, is obtained from a fit to $\sqrt{s_{NN}} = 200$ GeV data [75].

mental results for pions and kaons, that are not largely affected by the weak decays of the hyperons, agree with high precision. The solid (dotted) lines show the hydrodynamical results from [V] with $T_{\rm dec} = 150$ (120) MeV. The contributions from the hyperon feed-down are not included in the hydrodynamical results.

As in the case when collisions energy $\sqrt{s_{NN}} = 130$ GeV, as presented in Fig. 4.4 and discussed earlier, a rather good overall description of the measured spectra of identified hadrons is obtained using a single decoupling temperature $T_{\rm dec} = 150$ MeV, while all spectra are too shallow if $T_{\rm dec} = 120$ MeV is chosen. In particularly, Fig. 4.8 shows that the spectra of (positive) pions are very well reproduced using $T_{\rm dec} = 150$ MeV. Pions form ~ 75 % of the total multiplicity at RHIC at $y = 0$ (see Table 4.2) and thus are the most important constituents of the fireball.

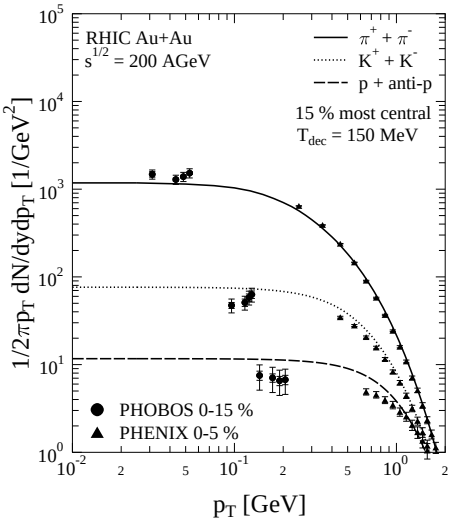

Figure 4.9: Transverse momentum spectra of charged pions and kaons and protons + anti-protons at $y = 0$ in the 15 % most central Au+Au collisions at $\sqrt{s_{NN}} = 200$ GeV calculated with $T_{\rm dec} = 150, 140, 130$ and 120 MeV. Data in the ultralow-p_T region is measured by PHOBOS [93]. Also shown is the PHENIX data [49] extending to larger p_T. Note the different centrality classes in the two data sets.

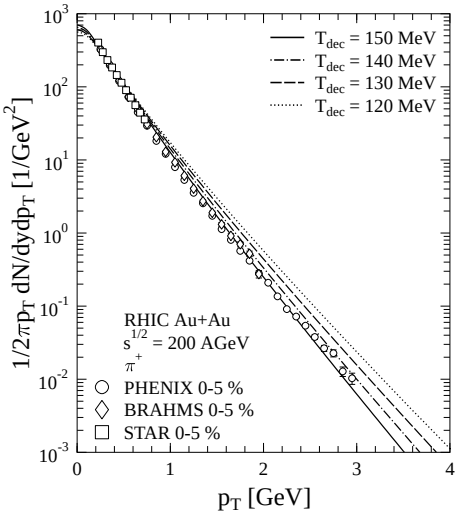

Figure 4.10: Spectrum of positive pions, measured by the PHENIX [49], STAR [50] and BRAHMS [53] collaborations, in the 5 % most central Au+Au collision at $\sqrt{s_{NN}} = 200$ GeV. The curves are the hydrodynamical results with $T_{\rm dec} = 150, 140, 130$ and 120 MeV.

Fig. 4.9 shows the spectra of $\pi^+ + \pi^-$, $\mathrm{K}^+ + \mathrm{K}^-$ and $\mathrm{p} + \bar{\mathrm{p}}$ at the ultra-low transverse momentum as measured by the PHOBOS collaboration in the 15 % most central Au+Au collisions at $\sqrt{s_{NN}} = 200$ GeV [93] . The data extending to higher p_T is by PHENIX. The hydrodynamical results are calculated with $T_{\mathrm{dec}} = 150$ MeV. By magnifying the small p_T scale, the over-shooting obtained in the kaon and (anti)proton yields can be seen. Pions are also well reproduced at low p_T and the transverse momentum plotted using a log-scale clearly depicts that the spectra of pions also become flat in the region $p_T \lesssim m_\pi$.

As seen from Fig. 4.8, the measured spectra of protons are flatter than the hydrodynamical results with $T_{\mathrm{dec}} = 150$ MeV. In the framework considered here the model has been kept as simple and transparent as possible. The overall description obtained at RHIC energies is, in fact, surprisingly good. In order to study the effects from the choice of the decoupling in more detail, the spectra of pions and protons will be shown when the decoupling temperature is varied between $120 - 150$ MeV in steps of 10 MeV.

Fig. 4.10 shows the measured [49, 50, 53, 92] spectra of positive pions already presented in Fig. 4.8 together with the hydrodynamical results with $T_{\mathrm{dec}} = 120, 130, 140$ and 150 MeV. The slopes of the measured pion spectra agree with the hydrodynamical results when $T_{\mathrm{dec}} = 140 \ldots 150$ MeV.

The measured spectra of protons are shown using two figures due to the details of feed-down contributions. Fig. 4.11 shows PHENIX [49] results where the feed-down is extracted from the data and Fig. 4.12 shows results obtained by STAR [50] and BRAHMS [92] with feed-down contributions. The hydrodynamical curves are calculated correspondingly. As discussed in Sec. 4.2, STAR obtains a larger multiplicity for protons than does BRAHMS. The data presented in Fig. 4.12 may suggest that a blast wave fit, used by STAR [50] to obtain the multiplicity, gives a rather flat transverse spectrum for protons.

As seen from Figs. 4.11 and 4.12, the hydrodynamical results tend to be too steep when $T_{\mathrm{dec}} = 140 \ldots 150$ MeV. With a lower decoupling temperature there would be an overshoot of the pion spectra and also the normalization of the proton spectrum would become too low. By choosing $T_{\mathrm{dec}} = 140$ MeV it appears that the RHIC data at $\sqrt{s_{NN}} = 200$ GeV is best described. However, a detailed simultanous description of both pion and proton spectra cannot be obtained from this calculation by assuming simultanous chemical and kinetic decoupling.

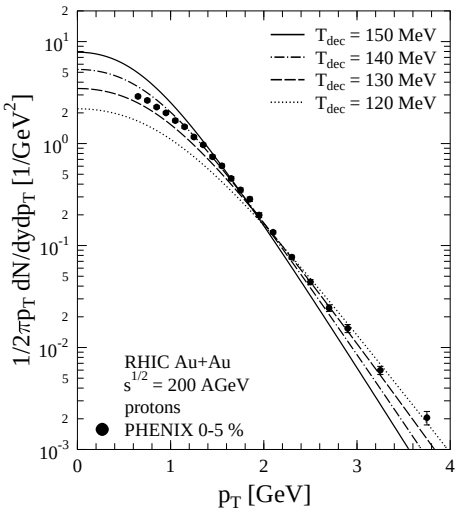

Figure 4.11: Transverse Spectrum of protons, measured by PHENIX [49], in the 5 % most central Au+Au collision at $\sqrt{s_{NN}} = 200$ GeV. The curves are the hydrodynamical results with $T_{\rm dec} = 150, 140, 130$ and 120 MeV. The PHENIX data is corrected for the weak hyperon decays and the hydrodynamical results are given without feed-down contributions.

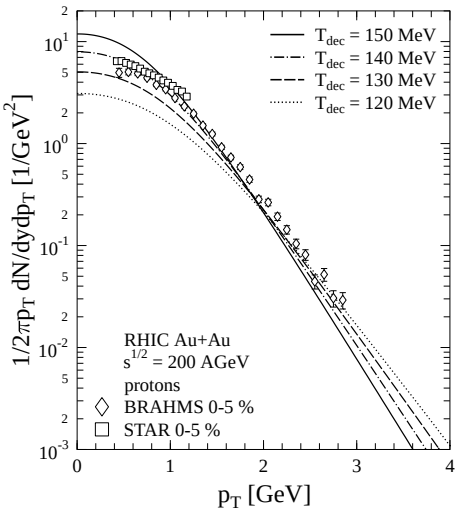

Figure 4.12: As in Fig. 4.11 but the data is taken by the STAR [50] and BRAHMS [92] collaboration. Both data and the hydrodynamical results include feed-down contributions.

Separate chemical freeze-out at temperature $T_{\rm chem} < T_{\rm kin}$ has been studied in [94, 34, 84]. With separate chemical freeze-out, a better description of (anti)proton spectra is found. However, construction of the EoS with partial chemical equilibrium is not unique [34] and requires modelling. It has been shown here that the main features of the Au+Au collisions at RHIC energies can be reproduced in a simple framework where $T_{\rm chem} = T_{\rm kin} \sim 150$ MeV, but the details of the spectra of heavy hadrons indicate a need for a more elaborate description of the hadron gas phase. Another possibility would be to treat the evolution after the chemical freeze-out and the decoupling e.g. with the hadronic transport model [95]. A detailed study of the effects from the chemical decoupling in the pQCD+saturation+hydrodynamics framework is beyond the intended scope here but should be addressed in the future.

4.3.2 Predictions for the LHC

Since the framework here for the initial state is closed, predictions can be made for hadron spectra at the LHC. The results for total (charged) multiplicity and transverse energy have already been presented in [I] using $T_{\rm dec} = 120$ MeV, as was discussed in Sec. 4.2. In what follows, the dependence of hadron spectra and multiplicities on the decoupling temperature is shown and discussed at the LHC energy.

Fig. 4.13 shows the results from [V] for spectra of charged particles in the

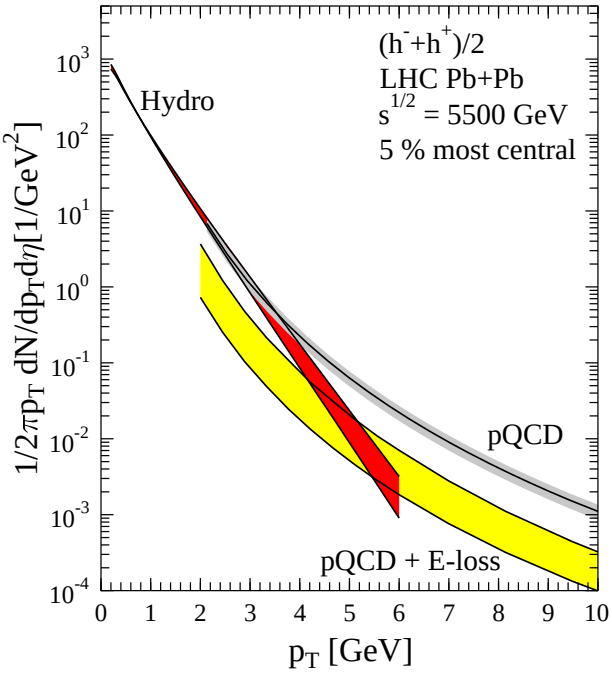

Figure 4.13: The prediction from [V] for the transverse momentum spectra of charged hadrons at $\eta = 0$ in the 5 % most central Pb+Pb collisions at the LHC energy $\sqrt{s_{NN}} = 5500$ GeV. The shaded band in the hydrodynamic results shows the sensitivity of the results to $T_{\rm dec}$ in the interval $150 \ldots 120$ MeV. The solid curve labeled "pQCD" corresponds to the pQCD fragmentation results, where no energy losses have been taken into account. The shaded band related to this is the estimated uncertainty in the extrapolation of the K-factor to the LHC energy. The shaded band labeled "pQCD + E-loss" describes the uncertainty in the pQCD fragmentation results with energy losses, see the text for details.

5 % most central Pb+Pb collisions at $\sqrt{s_{NN}} = 5500$ GeV. The hydrodynamical results are plotted as a red band which shows the sensitivity of the

results to the choice of $T_{\rm dec}$ in the range $120-150$ MeV. The curve labeled as "pQCD" shows results from jet fragmentation without energy loss. The grey band around the curve indicates the uncertainty in the energy dependent K-factor, when extrapolation to the LHC energy is done. The details are discussed in [V]. The yellow band represents the jet fragmentation calculation when energy losses are taken into account. The uncertainties in the yellow band account for only the reweighting of the quenching weights. In addition, there is a ~ 30 % "systematic" uncertainty which stems from the value of the K-factor.

As at RHIC, the hydrodynamical spectra of pions are not sensitive to $T_{\rm dec}$ in the range $p_T \lesssim 2$ GeV and hence the total multiplicity and transverse energy are also fairly insensitive to the decoupling temperature (see Table 4.5 below). Since the hydrodynamical spectra are considerably flatter than at RHIC, the thermal component of the spectra dominates up to $p_T \sim 4-5$ GeV. This suggests a larger applicability region for hydrodynamics at the LHC as compared to RHIC.

Fig. 4.14 shows the hydrodynamical results from [V] for the spectra of positive pions and kaons and protons. The solid curves correspond to $T_{\rm dec} = 150$ MeV chosen on the basis of the RHIC data. The sensitivity of these results to the choice of the decoupling temperature is illustrated by the yellow bands enveloping the curves. The steepest spectra are obtained by choosing $T_{\rm dec} = 160$ MeV and the most shallow ones with $T_{\rm dec} = 120$ MeV.

The integrated observables, the total multiplicities and transverse energies, and the multiplicities of different hadron species are given in Table 4.5 for three decoupling temperatures. A prediction of the pQCD+saturation model for the net-baryon number at mid-rapidity is also given.

The total charged multiplicity $dN^{\rm ch}/dy \sim 2850$ for the 5 % most central Pb+Pb collision at LHC energy $\sqrt{s_{NN}} = 5500$ GeV is predicted. This value is roughly three times higher than at RHIC. The ratio between the total transverse energy and multiplicity

$$R_{E_T N} \equiv \frac{dE_T/dy}{dN/dy} \tag{4.4}$$

is $R_{E_T N} \sim 0.63$ GeV at RHIC while at the LHC $R_{E_T N} \sim 0.86$ GeV which also indicates stronger transverse flow and larger average transverse energies of particles at the LHC compared to RHIC.

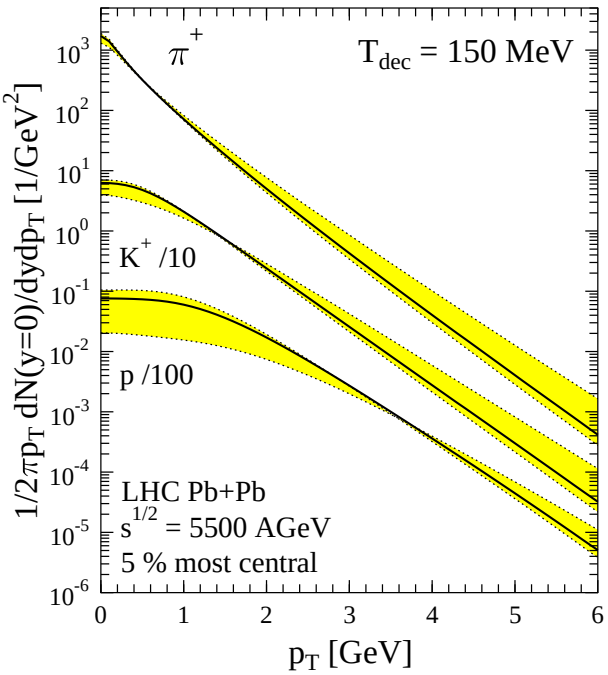

Figure 4.14: Transverse momentum spectra predicted for positive pions, positive kaons and protons at $y = 0$ in the 5 % most central Pb+Pb collisions at $\sqrt{s_{NN}} = 5500$ GeV. The solid lines show the hydrodynamic results with $T_{\rm dec} = 150$ MeV. The yellow envelopes around the curves represent varying $T_{\rm dec}$ in the range 120-160 MeV.

Proton multiplicity is difficult to predict, since the results vary by ~ 20 % even in the range of $T_{\rm dec} = 150 - 160$ MeV. Despite this, it is predicted that the net-baryon number will be as small as ~ 3 and the net proton number $\mathrm{p} - \bar{\mathrm{p}} \sim 1$, regardless of the decoupling temperature. Proton to anti-proton ratio, $\mathrm{p}/\bar{\mathrm{p}}$, is not very sensitive to the choice of $T_{\rm dec}$ at the LHC. This assertion can be justified through Eq. (4.3): $\Delta B/3\mathrm{p}$ is small for any $T_{\rm dec}$.

Some predictions for the total multiplicity at the LHC have been collected in [96]. At that time the expectations for the total multiplicity varied by a factor of 6, in the range $dN/dy \sim 1200 - 8000$! The RHIC data and further development of models, however, has reduced the spread in the predictions. A Monte Carlo-based event generator DPMJET, which is able to describe various collisions and observables, has predicted[4] $dN^{\rm ch}/dy \sim 2800$ [97]. A colour glass condensate model [37] is extended to the LHC energy [98] and the authors find that $dN^{\rm ch}/dy \sim 1750 - 2100$. A model which combines soft production and saturation of perturbatively produced minijets [99] gives

[4]The DPMJET-II.5 version of the code.

$T_{\rm dec}$ [MeV]	120	150	160
dN/dy(tot)	4460	4730	4840
$dN/d\eta$(tot)	4120	4240	4290
dN/dy(char)	2760	2850	2900
$dN/d\eta$(char)	2560	2570	2600
dE_T/dy(tot) [GeV]	4010	4070	4110
$dE_T/d\eta$(tot) [GeV]	3790	3710	3680
dN^{π^+}/dy	1170	1120	1120
dN^{π^0}/dy	1290	1240	1240
dN^{π^-}/dy	1170	1120	1120
$dN^{\rm K^+}/dy$	175	214	218
$dN^{\rm K^-}/dy$	175	214	218
$dN^{\rm p}/dy$	25.8	70.8	88.1
$dN^{\bar{\rm p}}/dy$	24.6	69.6	86.9
$\bar{\rm p}/{\rm p}$	0.95	0.98	0.99
$dN_{B-\bar{B}}/dy$		3.11	

Table 4.5: Multiplicities and total transverse energies without feed-down contributions for the 5 % most central Pb+Pb collisions at $\sqrt{s_{NN}} = 5500$ GeV. A prediction for the net-baryon number is also shown.

$dN^{\rm ch}/dy \sim 3000 - 3300$. As there is still a factor of two spread in the range of these prediction values, the forthcoming LHC data will be eagerly awaited.

4.4 Thermal photons

Thermal photons are suggested to be an ideal probe for the hot early stages of the evolution, since photons escape from the collision region immediately after production, due to their large mean free path [56]. However, as discussed in Sec. 2.7.1, the measured photon spectrum is composed of photons from various sources of electromagnetic interaction that occurs in all stages of the collision. The dominant contribution comes from decays of the final state hadrons, mainly π^0's and η's, which makes the isolation of excess photons, over those originating from the decays of final hadrons, an experimentally challenging task. The WA98 collaboration [28, 29] has succeeded in producing results on excess photons at the SPS. Recently, the PHENIX collaboration [100] has also reported on spectra of excess photons at RHIC.

The excess photons consists of prompt photons from interactions between

partons of incoming nuclei, photons from jet-photon conversion [65] and thermal photons from secondary interaction in the expanding fireball.

4.4.1 The WA98 data

It seems that the WA98 data [28, 29] for excess photons cannot be fully explained with prompt photons [101, 29]. This means there is room for thermal photons, from secondary interactions, in the explanation. In [II] thermal photons, with a (2+1)-dimensional hydrodynamical software, in Pb+Pb collision at $\sqrt{s_{NN}} = 17.3$ GeV were analyzed. The code includes both transverse and longitudinal expansion but assumes azimuthal symmetry. Obtained results were compared to those found using (1+1)-dimensional boost-invariant hydrodnamics[5].

As discussed in Sec. 3.4, the initial state for boost-invariant (BI) hydrodynamics cannot be obtained, at the SPS energies, from the pQCD+saturation model. Hence, the shapes of the initial density profiles for BI-hydrodynamics from [87], which were given at the thermalization time $\tau_0 = 0.8$ fm/c, were used. This initial state was scaled to $\tau_0 = 1.0$ and 0.3 fm/c with a longitudinal Bjorken expansion such that the entropy in the unit rapidity remained constant.

The justification for scaling up the thermalization time to $\tau_0 = 1.0$ fm/c is to fulfill the condition on the transit time of the colliding nuclei, as presented in Sec. 3.4, on which basis $\tau_0 = 1.0$ fm/c is chosen in many hydrodynamical studies at the SPS energies. Scaling to $\tau_0 = 0.3$ fm/c was inspired by the studies presented in [102], in which the authors found that the initial state, with $\tau_0 = 1.0$ fm/c, cannot reproduce the high-k_T region of the excess photon spectrum without an initial transverse velocity. However, lowering the initial time leads to better description of the photon spectrum. This can be understood as follows [102, II, IV]: the total entropy (in the central rapidity unit) of the initial state can be fixed from the experimental multiplicity, i.e. normalization of the initial entropy density for a chosen thermalization time τ_0. Small changes in τ_0 do not alter the final hadron spectra appreciably as long as the total initial entropy is the same (see Fig. 4.16 below). In the case of a massless ideal gas, without radial expansion, the temperature scales as $T(r,\tau) = T(r,\tau_0) \times (\tau/\tau_0)^{1/3}$ meaning, that decreasing the thermalization time considerably raises the initial temperature. This, however, leads to an enhancement in the thermal photon spectrum at high photon transverse

[5] The author has performed the boost-invariant calculations in [II] and thus the results from this simpler approach are discussed in a more detailed fashion.

momentum, k_T, due to Boltzmann suppression $\sim e^{-k_T/T}$ in the emission rates.

The authors of [103] have studied an interplay between the thermalization time and a possible initial radial velocity in the spectra of thermal photons at the SPS. They made a simultaneous χ^2-analysis of the hadron spectra and the WA98 data. The outcome was that the thermalization time can be raised to $\tau_0 \gtrsim 1.0$ fm/c by the introduction of an initial linear radial velocity. Although lowering the initial temperature reduces the photon emission in high-k_T region, the stronger radial velocity compensates for the effect by boosting the emitted photons to larger k_T [103, II].

The effects from thermalization time and initial radial velocity are summarized in Fig. 4.15. The red (blue) solid (dashed) line shows the results with

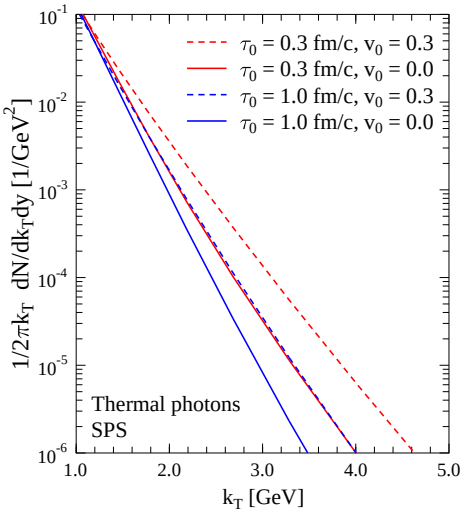

Figure 4.15: Transverse momentum spectra of thermal photons at the SPS assuming $\tau_0 = 1.0$ or 0.3 fm/c and $v_r = 0$ or 0.3.

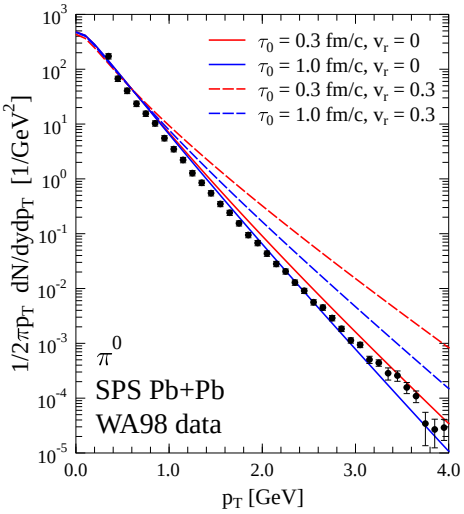

Figure 4.16: Transverse momentum spectra of neutral pions at the SPS measured by the WA98 collaboration [28, 29]. The curves are results from boost invariant hydrodynamics, assuming $\tau_0 = 1.0$ or 0.3 fm/c and $v_r = 0$ or 0.3.

$\tau_0 = 0.3$ (1.0) fm/c and $v_r = 0$ (0.3). As discussed above, and shown in Fig. 4.15, the combination of $\tau_0 = 0.3$ fm/c with $v_r = 0$ and $\tau_0 = 1.0$ fm/c with $v_r = 0.3$ leads to exactly the same thermal photon spectrum. Two-loop photon emission rates [59] are used in the plasma phase in the calculations presented in Fig. 4.15. The hydrodynamical results are compared to the

WA98 data below in Fig. 4.17. In those results, the resummed photon emission rate [61], which includes the LPM suppression, is used.

In summary, in order to use boost-invariant hydrodynamics to explain WA98 data, either a fast thermalization need to be assumed or an initial radial velocity need to be introduced. Unfortunately, both possibilities contain unsatisfactory elements at the SPS. A rapid thermalization at $\tau_0 \sim 0.3$ fm/c violates the estimated transit time of the nuclei, indicating that the hydrodynamical evolution begins while the fireball is still in formation.

The spectrum of neutral pions measured by the WA98 collaboration [28, 29] is shown in Fig. 4.16. The curves show the results from boost-invariant hydrodynamics with $\tau_0 = 0.3$ (1.0) fm/c and $v_r = 0$ (0.3), as in Fig. 4.15. The results verify the statement that the slope of the pion spectrum does not change significantly when the initial time τ_0 is reduced from 1.0 fm/c (solid blue line) to 0.3 fm/c (solid red line). As seen from Fig. 4.16, the slopes of the pion spectra do not tolerate an initial radial velocity of $v_r = 0.3$ (dashed lines) in the calculations but instead, lead to an overshooting[6] as compared to the WA98 data [28, 29]. These observations may indicate, that the boost-invariant description fails to explain the WA98 results for the thermal photons simultanously with the π^0 data, and it is essential to take into account the longitudinal geometry at the SPS. However, this study is "conservative" in the sense that effects from the in-medium modification of hadrons, studied e.g. in [104], are not taken into account.

The results from [II] for studies of the WA98 data have been collected and presented in Figs. 4.17 and 4.18. The labels "IS 1" and "IS 2" refer to the two initial states used in the (2+1)-dimensional hydrodynamical code, in which the assumption of the boost-invariance is relaxed. These initial states are described in detail and the results for hadronic observables are shown in [25, II]. IS 1 is such that the initial energy density is strongly peaked in the middle of the fireball, leading to a large value for the maximum initial temperature. In IS 2, the initial densities are flatter and hence, the temperature is also smaller. All calculations were done using EoS which has a phase transition to the QGP (referred to as "EoS A" below).

Curves labeled as "BI" in Fig. 4.17 show results from the boost-invariant hydrodynamics. The number in the parenthesis refers to the initial time, $\tau_0 = 0.3$ or 1.0 fm/c. If compared to the results shown in Fig. 4.15 (with $v_r = 0$), it can be seen that the thermal photon yield is reduced by ~ 30 %

[6] One should note that similar overshooting did not occur in [103].

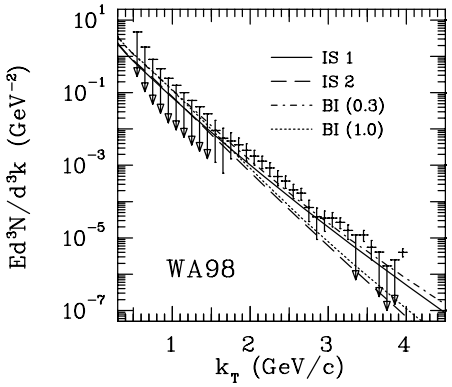

Figure 4.17: Thermal photon spectra at the SPS from [II] with WA98 data [28, 29]. Curves labeled as "IS 1" and "IS 2" show results from non-boost-invariant hydrodynamics with two different initial conditions. Label "BI" refers to boost-invariant hydrodynamics and the number in parenthesis to initial times $\tau_0 = 0.3$ and 1.0 fm/c. EoS A, with a phase transition to QGP, was used in all calculations.

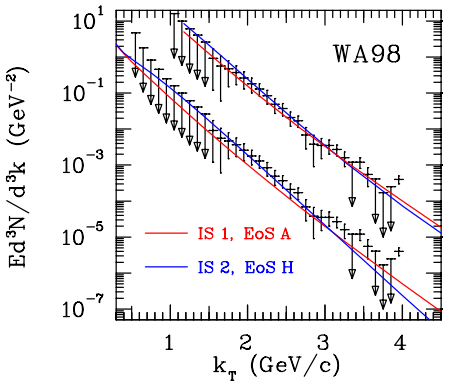

Figure 4.18: The lower set of curves as in Fig. 4.17 but EoS A (H) refers to EoS with (without) a phase transition. The upper set of curves, scaled by a factor of 100, shows the results when the contribution from the prompt photons [101] is included.

when the LPM suppression [60, 61] is included in the photon emission rate.

A "hot" initial state, IS 1, leads to a similar result as BI(0.3), where the thermalization time in boost invariant hydrodynamics is pushed to values which contradict the longitudinal geometry. Similarly, a "cool" initial state, IS 2, is close to the case of BI(1.0) which is in accordance with the longitudinal geometry. It is clear that, either IS 2 + EoS A or BI(1.0) can reproduce the high-k_T region of the excess photon spectrum.

It is important to note that, contrary to BI(0.3), the initial state IS 1 is *realistic*. In the case where the assumption of boost invariant flow is relaxed and the system has an initial finite longitudinal extent, the initial thermalization time is no longer uniquely defined. However, an estimate of the thermalization time can be made from the initial longitudinal extent of the fireball: as the Lorentz gamma factor $\gamma \sim 10$ at the SPS, the thickness of the system is roughly ~ 1.3 fm when the colliding nuclei have maximum overlap. The time taken to reach the longitudinal extent of 3.4 fm, which was chosen in [II], would be ~ 1 fm/c.

Fig. 4.18 shows the results for the thermal photon emission for the combinations IS 1 + EoS A and IS 2 + EoS H. While there is a phase transition to QGP in the EoS A, the EoS H describes the matter as a hadron gas at all temperatures[7]. The upper set of curves in Fig. 4.18, scaled up by a factor of 100, include contributions from the prompt photons [101]. Combinations IS 1 + EoS A and IS 2 + EoS H simultaneously reproduce [25, II, IV] the NA49 data [105] for the rapidity distributions of negative hadrons and the WA98 data [28, 29] for neutral pions and direct photons. As discussed in [II, IV], the initial temperature is ~ 50 MeV higher in IS 1 as compared to IS 2 due to a different choice for the initial longitudinal flow. Yet, the final flow conditions and the entropy of the initial state are so similar, that the hadronic data is equally well reproduced. Although the parameter space for the initial conditions, that reproduce the hadronic observables, is large, it can be restricted by using electromagnetic observables as anticipated in [25].

In summary, when the assumption of boost-invariant flow is relaxed, one can find realistic initial conditions which well describe both hadronic and direct photon data. Also, even the average initial temperature has to be considerable, $\langle T_{\rm ini} \rangle \gtrsim 210$ MeV [II, IV], and above the critical temperature obtained from the lattice [3, 38]. The shape of the direct photon spectrum is better reproduced in the scenario with a phase transition. These observations lend support for plasma formation at the SPS but uncertainties — both theoretical and experimental — are too large to draw a definite conclusion. Nonetheless, the assumption of plasma formation does not contradict experimental results.

4.4.2 Thermal photons at RHIC

As discussed in the introduction of [V] (see also the citations presented), there is a wealth of evidence that the energy density obtained at RHIC is considerably higher than at the SPS. As thermal photon emission is very sensitive to the initial temperature, it is particularly interesting to study it in the context of fast thermalization as assumed here.

A prediction for the thermal photon emission in the 6 % most central Au+Au collisions at $\sqrt{s_{NN}} = 200$ GeV was presented in [IV]. Since the data taken by PHENIX [100] is for the 10 % most central collisions, the results here are presented with the same centrality selection. However, the difference in the results is rather small.

[7] EoS H is the same as "HRG" in [III] used in order to study the evolution of $T_{\rm eff}$.

Figs. 4.19 and 4.20 show the prediction from [IV] for thermal photons together with the PHENIX data [100]. To see the difference between the centralities of 0-6 % and 0-10 %, compare Fig. 4.19, which shows the results in the 6 % most central collisions as predicted in [IV], and Fig. 4.20, where the 0-10 % centrality is used.

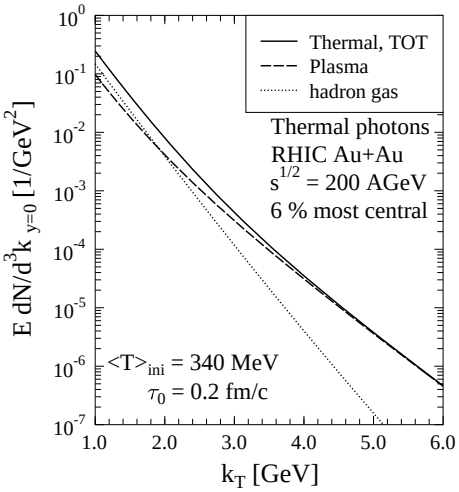

Figure 4.19: The prediction from [IV] for transverse momentum spectra of thermal photons in the 6 % most central Au+Au collisions at $\sqrt{s_{NN}} = 200$ GeV. Plasma refers to the contribution from QGP and QGP part of the mixed phase. Likewise for the hadron gas contribution.

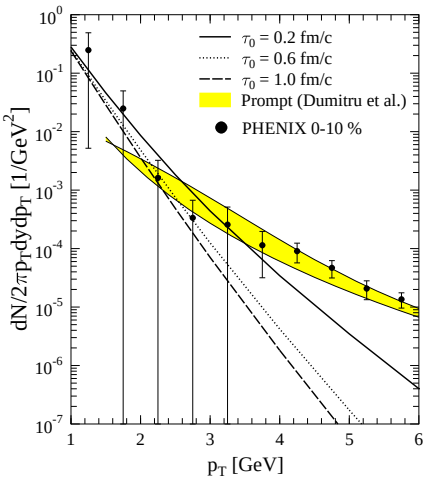

Figure 4.20: Transverse momentum spectra of excess photons in the 10 % most central Au+Au collisions at $\sqrt{s_{NN}} = 200$ GeV by the PHENIX collaboration [100]. The solid line is a prediction of the framework considered in the text. The dashed (dotted) line is obtained when the thermalization time is scaled down to $\tau_0 = 0.6$ (1.0) fm/c. The yellow band shows a prediction for the contribution from prompt photons [106]. The upper limit is obtained by assuming intrinsic transverse momentum $\langle p_T^2 \rangle = 2.4$ GeV^2. In the lower limit $\langle p_T^2 \rangle = 0$.

The solid line in Fig. 4.19 shows the total thermal photon spectrum and the dashed (dotted) line presents the contribution from the plasma (hadron gas) phase. Emission from the plasma (hadron gas) part of the mixed phase is included in the dashed (dotted) line. The contribution from the plasma dominates the spectrum of thermal photons at $k_T \gtrsim 3$ GeV. However, this results from the assumption of an early thermalization, which leads to a large initial temperature. If $\tau_0 = 1.0$ fm/c is assumed, emission from the

hadron gas and plasma are of equal importance.

Fig. 4.20 shows the transverse momentum spectra of excess photons in the 10 % most central Au+Au collisions at $\sqrt{s_{NN}} = 200$ GeV as measured by the PHENIX collaboration [100]. Once again, the solid line is a prediction of the pQCD+saturation+hydrodynamics framework. The dotted (dashed) line shows the results when the thermalization time is scaled to $\tau_0 = 0.6$ (1.0) fm/c. A prediction for the prompt photon contribution [106] is also shown as a yellow band in Fig. 4.20. The upper limit is obtained by assuming an intrinsic transverse momentum of $\langle p_T^2 \rangle = 2.4$ GeV^2, while in the lower limit $\langle p_T^2 \rangle = 0$.

As can be seen from Fig. 4.20, a drop of the initial temperature (i.e. late thermalization) drastically reduces the photon emission. Also, the high-k_T region of the thermal photon spectrum in the case $\tau_0 = 0.6$ fm/c is clearly closer to the results using $\tau_0 = 1.0$ fm/c than the ones obtained with $\tau_0 = 0.2$ fm/c. This further demonstrates the fact that the dominant contribution to the high-k_T region of the thermal photon spectra comes from the first moments of the evolution. As the studies at SPS energies showed, the choice of the thermalization time is indeed the biggest uncertainty when boost-invariant hydrodynamics is used to calculate the thermal photons spectrum.

More statistics is needed to obtain clear experimental results at $k_T \lesssim 3$ GeV region, where so far only 90 % confidence upper limits have been achieved [100]. The latest preliminary results presented at the Quark Matter 2005 conference [107] indicate that the data will be consistent with these upper limits. The prompt photons dominate the excess photon spectrum in the region $p_T \gtrsim 3$ GeV. Hence, more accurate data around $k_T \sim 2$ GeV will be useful in studying the thermal emission.

The results with $\tau_0 = 1/p_{\mathrm{sat}}$ (solid line in Fig. 4.20) are consistent with the upper limits obtained by the PHENIX collaboration. Also, this calculation should give an upper limit for the thermal photon emission as the matter was assumed to thermalize immediately after production. The studies of the elliptic flow indicate that τ_0 should be smaller than 1.0 fm/c and hence, choosing $\tau_0 = 1.0$ fm/c can be considered as a lower limit. Uncertainties in the experimental results are considerable at the low-k_T region but the upper limits obtained suggest that a change of the slope takes place when the prompt photon contribution begins to dominate the spectra at $k_T \sim 3$ GeV, as was predicted in [IV].

The contribution from the jet photon conversion [65] has been recently studied in more detail in [66] and found to be of the same magnitude as with prompt photons at $k_T \sim 2.5$ GeV. Nevertheless, both seem to fall under the thermal production at $k_T \lesssim 2$ GeV.

As discussed in Sec. 4.1, it is known that the created minijet system is mostly gluonic and hence it may be far from thermal equilibrium. As there are less degrees of freedom in the gluon rich plasma, the temperature as a function of energy density is larger. However, at the same time the emission rate is reduced as there are less charged (anti)quarks in the plasma. A detailed study of equilibration of the plasma and photon emission in non-equilibrium, based on the initial state obtained from the pQCD+saturation model, was presented in [67]. Details of the study are beyond the scope of discussion here. However, the final outcome is that the rise in the temperature and the reduction of the emission rate cancel each other out to large extend. Publication [67] also presents the predictions for the thermal photon emission at the LHC.

Chapter 5

Discussion and Outlook

Boost-invariant hydrodynamical studies, in which the initial state is based on the pQCD+saturation model [17] at collider energies, were presented in this thesis. In most of the hydrodynamical studies the initial state is obtained with a trial and error method using experimental data as a feed-back. Although a lot can be learnt about the properties of the dense medium with these studies, the predictive power of the hydrodynamical model is limited, since the hydrodynamics itself cannot be used to study the formation of the dense fireball in high energy collisions.

The pQCD+saturation model is a description of particle production in primary interactions between the partons of the incoming nuclei. By assuming an adiabatic longitudinal expansion, the pQCD+saturation model has successfully predicted the multiplicities observed in the central collisions at the RHIC energies. However, as the model [17] does not include transverse expansion, a collective transverse flow or the transverse spectra of hadrons, for example, cannot be studied. A more realistic equation of state and a space-time evolution determined by boost-invariant hydrodynamics with the transverse expansion was considered in [I, III, V].

Together, the assumptions of fast thermalization and entropy conservation, during the expansion, relate the final rapidity density of hadrons to the number of partons produced to mid-rapidity unit in the primary interactions [17]. Because of entropy conservation, details of the transverse expansion do not affect the results for the multiplicities. The situation is more complicated for the transverse energy. The initial transverse energy of the produced partons is large but it is reduced by the pdV work done in the longitudinal expansion [17]. The collective transverse flow partly compensates for this reduction but it is still considerable: a factor of 2.7 at RHIC and 3.6 at the

LHC [I].

Hadron spectra in the 5 % most central Au+Au collisions at $\sqrt{s_{NN}} = 130$ GeV were studied in [III]. It was found that the experimentally measured spectra favour a high decoupling temperature, $T_{\rm dec} \sim 150$ MeV, when simultaneous chemical and kinetic decoupling is assumed. The data taken at $\sqrt{s_{NN}} = 200$ GeV leads to the same conclusions [V]. The role of the high decoupling temperature has been discussed [III, V]. Also, the feed-down contributions, from the weak decays of hyperons, in the hadron spectra and multiplicities have been discussed in detail [V].

The measured spectra of charged particles are well reproduced in the transverse momentum range $p_T \lesssim 2$ GeV which is the same applicability region for a hydrodynamical description as suggested by the studies of elliptic flow [32]. The high-p_T region of the transverse spectra of charged hadrons can be described using jet fragmentation and energy loss calculations [V]. At RHIC, an intersection between the hydrodynamical and jet fragmentation+energy loss spectra takes place at the intermediate $p_T \sim 3 \ldots 4$ GeV.

The measured spectra of pions are very well reproduced but the spectra of protons show interesting details. If the decoupling temperature is taken as $T_{\rm dec} \sim 150$ MeV, the proton spectrum is too steep and the normalization is too large. With a smaller decoupling temperature the pion spectra become too shallow and the proton yield too small. These observations indicate a need for separate chemical and kinetic decoupling. As studied in [94, 34, 84], when the chemical decoupling is considered, the spectra of pions no longer depend on the choice of the kinetic freeze-out temperature and the chemical potentials preserve the normalization of the proton spectra. With a kinetic decoupling temperature $T_{\rm kin} \sim 100$ MeV the proton spectra become more shallow, in accordance with the measured data. However, the bulk properties of the created fireball can be described with the simpler framework considered here.

As the initial state of the hydrodynamics is determined from the pQCD+ saturation calculation, the studies can be easily extended to the LHC energy [I, V]. Predictions for the transverse spectra and integrated observables at the LHC energy were presented. In particular, the predictions for the charged particle multiplicity $dN_{ch}/dy = 2850$, the net baryon number $N_B - N_{\bar{B}} = 3.14$ and for the net proton multiplicity $\mathrm{p} - \bar{\mathrm{p}} \approx 1$, at the central rapidity unit, are fairly insensitive to the decoupling temperature. Also, the crossing of hydrodynamical and jet fragmentation+energy loss results takes

place at $p_T \sim 4 \ldots 6$ GeV at the LHC. This indicates a wider applicability region for the hydrodynamical models at the LHC compared to RHIC. In particular, the elliptic flow should follow the hydrodynamical description up to a larger transverse momentum at the LHC.

Thermal photons are penetrating probes and the high photon transverse momentum range of the thermal photon spectra are sensitive to the first moments of the evolution, i.e. to the initial conditions of the hydrodynamical evolution. The thermal photon emission at the SPS has been studied [II] and it has been observed that the details of the longitudinal expansion can be important at these lower energies. At the RHIC energies, boost-invariant hydrodynamics should work better at the mid-rapidity region. However, at RHIC, the contribution from prompt photons [106] and jet photon conversion [66] exceeds the thermal component in the large transverse momentum region, where the contribution from the plasma phase dominates the thermal emission. Nevertheless, it seems that a possible window exists at $k_T \sim 2$ GeV where the thermal component dominates the direct photon spectra.

A prediction for the excess photon spectrum has been presented [IV]. The thermal emission was calculated with the initial conditions from the pQCD+ saturation model. The sensitivity to the thermalization time was also studied. The prompt photon contribution was taken from a prediction presented in [106]. By combining these results, good agreement with the data gathered by the PHENIX collaboration [100] was obtained. At $k_T \sim 2$ GeV, the prediction from [IV] with the assumption of fast thermalization, $\tau_0 = 1/p_{\rm sat}$, is close to the experimental upper limits obtained in that region. Recent preliminary data [107] indicates that the final spectra will be close to the observed upper limits.

As discussed, the measured proton spectra and particle ratios, in particular, indicate the presence of a separate chemical decoupling. This also leads to effects on the thermal emission of photons in the hadronic phase. In the case of a partial chemical equilibrium, the temperature, in a given energy density, is smaller than in the case of equilibrium [94, 34, 84] and the final size of the system at decoupling is smaller for a given decoupling temperature [34, 84]. Hence, a reduction of the emission from the hadron phase can be expected. This should be studied in detail in future.

At collider energies, a fast thermalization, immediately after the primary production has taken place, has been assumed. Plasma instabilities [81] lend support for a faster thermalization as compared to the estimate $\tau_{\rm therm} \sim 2{-}3$

fm/c, at the RHIC energies, obtained from bottom-up description [82]. However, values such as $\tau_{\rm therm} \sim 0.6$ fm/c, which are commonly assumed in the hydrodynamical studies at the RHIC energies, also are "considerably smaller" in this respect.

Based on the pQCD+saturation model, the matter created in the primary interaction is mostly gluonic. The deviation from the chemical equilibrium has been described using multiplicative fugacities in [88, 89, 108, 67], and predictions for the thermal photon emission at the LHC energy are also made [67]. It was found that the lifetime of the plasma phase is long enough for the fireball to nearly reach chemical equilibrium before hadronization. However, chemical equilibration may happen within a considerably smaller timescale. The production of quark-anti quark pairs in the presence of strong colour fields has been studied recently [109]. It seems that $q\bar{q}$-pairs are produced abundantly at a rapid rate and thus, the production of pairs through the inelastic scatterings, like $gg \rightarrow q\bar{q}$, may be less important in reaching the chemically equilibriated particle ratios.

In summary, the thermalization of the produced fireball is not yet fully understood. However, the formation time of a dense partonic system is $\tau_{\rm form} \sim 1/p_{\rm sat} \sim 0.2$ fm/c at the RHIC. Even if the matter is not thermalized immediately after the formation, there will be interactions among the produced partons before $\tau \sim 0.6$ fm/c. It is assumed here that these collisions can be effectively described by the immediate application of hydrodynamics after the formation. A similar argument can also be given for the description of photon emission from secondary interactions. If the matter is not thermalized, there would be an emission of pre-thermal photons from the scattering of partons, which leads to the thermalization. As a first approximation, these may be described with hydrodynamics by using the thermal emission rates.

Bibliography

[I] Publication I of this thesis.

[II] Publication II of this thesis.

[III] Publication III of this thesis.

[IV] Publication IV of this thesis.

[V] Publication V of this thesis.

[1] N. Cabibbo and G. Parisi, Phys. Lett. B **59** (1975) 67.

[2] J. C. Collins and M. J. Perry, Phys. Rev. Lett. **34** (1975) 1353.

[3] F. Karsch, Nucl. Phys. A **698** (2002) 199 [arXiv:hep-ph/0103314].

[4] A. K. Holme, E. F. Staubo, L. P. Csernai, E. Osnes and D. Strottman, Phys. Rev. D **40** (1989) 3735.

[5] K. Rajagopal, Nucl. Phys. A **661** (1999) 150 [arXiv:hep-ph/9908360].

[6] N. Itoh, Prog. Theor. Phys. **44** (1970) 291.

[7] B. Freedman and L. D. McLerran, Phys. Rev. D **17** (1978) 1109.

[8] K. A. Olive, Nucl. Phys. B **190** (1981) 483.

[9] J. D. Bjorken, Phys. Rev. D **27** (1983) 140.

[10] J. Adams *et al.* [STAR Collaboration], Phys. Rev. C **70** (2004) 054907 [arXiv:nucl-ex/0407003].

[11] S. S. Adler *et al.* [PHENIX Collaboration], Phys. Rev. C **71** (2005) 034908 [Erratum-ibid. C **71** (2005) 049901] [arXiv:nucl-ex/0409015].

[12] J. Adams *et al.* [STAR Collaboration], arXiv:nucl-ex/0409033.

[13] S. S. Adler *et al.* [PHENIX Collaboration], Phys. Rev. Lett. **94** (2005) 232302 [arXiv:nucl-ex/0411040].

[14] B. B. Back *et al.* [PHOBOS Collaboration], arXiv:nucl-ex/0407012.

[15] U. A. Wiedemann, Eur. Phys. J. C **43** (2005) 215 [arXiv:hep-ph/0503119].

[16] L. D. Landau, Izv. Akad. Nauk Ser. Fiz. **17** (1953) 51.

[17] K. J. Eskola, K. Kajantie, P. V. Ruuskanen and K. Tuominen, Nucl. Phys. B **570** (2000) 379 [arXiv:hep-ph/9909456].

[18] D. Teaney, Phys. Rev. C **68** (2003) 034913.

[19] A. Muronga, Phys. Rev. C **69** (2004) 034903 [arXiv:nucl-th/0309055].

[20] A. Muronga and D. H. Rischke, arXiv:nucl-th/0407114.

[21] G. Baym, B. L. Friman, J. P. Blaizot, M. Soyeur and W. Czyz, Nucl. Phys. A **407** (1983) 541.

[22] H. Von Gersdorff, L. D. McLerran, M. Kataja and P. V. Ruuskanen, Phys. Rev. D **34** (1986) 794.

[23] P. V. Ruuskanen, Acta Phys. Polon. B **18** (1987) 551.

[24] J. Sollfrank, P. Huovinen, M. Kataja, P. V. Ruuskanen, M. Prakash and R. Venugopalan, Phys. Rev. C **55** (1997) 392 [arXiv:nucl-th/9607029].

[25] J. Sollfrank, P. Huovinen and P. V. Ruuskanen, Heavy Ion Phys. **5** (1997) 321 [arXiv:nucl-th/9706012].

[26] J. Sollfrank, P. Huovinen and P. V. Ruuskanen, Eur. Phys. J. C **6** (1999) 525 [arXiv:nucl-th/9801023].

[27] P. Huovinen, P. V. Ruuskanen and J. Sollfrank, Nucl. Phys. A **650** (1999) 227 [arXiv:nucl-th/9807076].

[28] M. M. Aggarwal *et al.* [WA98 Collaboration], Phys. Rev. Lett. **85** (2000) 3595 [arXiv:nucl-ex/0006008].

[29] M. M. Aggarwal *et al.* [WA98 Collaboration], arXiv:nucl-ex/0006007.

[30] J. Y. Ollitrault, Phys. Rev. D **46** (1992) 229; Phys. Rev. D **48** (1993) 1132 [hep-ph/9303247].

[31] S. Voloshin and Y. Zhang, Z. Phys. C **70** (1996) 665 [arXiv:hep-ph/9407282].

[32] P. F. Kolb and U. W. Heinz, arXiv:nucl-th/0305084.

[33] T. Hirano, Phys. Rev. C **65** (2002) 011901 [arXiv:nucl-th/0108004].

[34] T. Hirano and K. Tsuda, Phys. Rev. C **66** (2002) 054905 [arXiv:nucl-th/0205043].

[35] T. Hirano, Acta Phys. Polon. B **36** (2005) 187 [arXiv:nucl-th/0410017].

[36] T. Hirano and Y. Nara, Nucl. Phys. A **743** (2004) 305 [arXiv:nucl-th/0404039].

[37] D. Kharzeev and E. Levin, Phys. Lett. B **523** (2001) 79 [arXiv:nucl-th/0108006].

[38] Z. Fodor and S. D. Katz, JHEP **0203** (2002) 014 [arXiv:hep-lat/0106002].

[39] F. Karsch, K. Redlich and A. Tawfik, Phys. Lett. B **571** (2003) 67 [arXiv:hep-ph/0306208].

[40] R. A. Schneider and W. Weise, Phys. Rev. C **64** (2001) 055201 [arXiv:hep-ph/0105242].

[41] P. Huovinen, Nucl. Phys. A **761** (2005) 296 [arXiv:nucl-th/0505036].

[42] F. Cooper and G. Frye, Phys. Rev. D **10** (1974) 186.

[43] P. V. Ruuskanen, Nucl. Phys. A **702** (2002) 259 [arXiv:nucl-th/0111057].

[44] J. Sollfrank, P. Koch and U. W. Heinz, Z. Phys. C **52** (1991) 593.

[45] K. Hagiwara *et al.* [Particle Data Group Collaboration], Phys. Rev. D **66** (2002) 010001.

[46] C. Adler *et al.* [STAR Collaboration], Phys. Rev. Lett. **89** (2002) 092301 [arXiv:nucl-ex/0203016].

[47] K. Adcox *et al.* [PHENIX Collaboration], Phys. Rev. Lett. **89** (2002) 092302 [arXiv:nucl-ex/0204007].

[48] K. Adcox *et al.* [PHENIX Collaboration], Phys. Rev. Lett. **88** (2002) 242301 [arXiv:nucl-ex/0112006].

[49] S. S. Adler *et al.* [PHENIX Collaboration], Phys. Rev. C **69** (2004) 034909 [arXiv:nucl-ex/0307022].

[50] J. Adams *et al.* [STAR Collaboration], Phys. Rev. Lett. **92** (2004) 112301 [arXiv:nucl-ex/0310004].

[51] K. J. Eskola, K. Kajantie and P. V. Ruuskanen, Eur. Phys. J. C **1** (1998) 627 [arXiv:nucl-th/9705015].

[52] K. Morita, S. Muroya, C. Nonaka and T. Hirano, Phys. Rev. C **66** (2002) 054904 [arXiv:nucl-th/0205040].

[53] I. G. Bearden *et al.* [BRAHMS Collaboration], Phys. Rev. Lett. **94** (2005) 162301 [arXiv:nucl-ex/0403050].

[54] I. G. Bearden *et al.* [BRAHMS Collaboration], Phys. Rev. Lett. **93** (2004) 102301 [arXiv:nucl-ex/0312023].

[55] T. Renk, Phys. Rev. C **71** (2005) 064905 [arXiv:hep-ph/0503082].

[56] M. H. Thoma, Phys. Rev. D **51** (1995) 862 [arXiv:hep-ph/9405309].

[57] J. I. Kapusta, P. Lichard and D. Seibert, Phys. Rev. D **44** (1991) 2774 [Erratum-ibid. D **47** (1993) 4171].

[58] R. Baier, H. Nakkagawa, A. Niegawa and K. Redlich, Z. Phys. C **53** (1992) 433.

[59] P. Aurenche, F. Gelis, R. Kobes and H. Zaraket, Phys. Rev. D **58** (1998) 085003 [arXiv:hep-ph/9804224].

[60] P. Arnold, G. D. Moore and L. G. Yaffe, JHEP **0111** (2001) 057 [arXiv:hep-ph/0109064].

[61] P. Arnold, G. D. Moore and L. G. Yaffe, JHEP **0112** (2001) 009 [arXiv:hep-ph/0111107].

[62] L. Xiong, E. V. Shuryak and G. E. Brown, Phys. Rev. D **46** (1992) 3798 [arXiv:hep-ph/9208206].

[63] H. Nadeau, J. I. Kapusta and P. Lichard, Phys. Rev. C **45** (1992) 3034.

[64] S. Turbide, R. Rapp and C. Gale, Phys. Rev. C **69** (2004) 014903 [arXiv:hep-ph/0308085].

[65] R. J. Fries, B. Muller and D. K. Srivastava, Phys. Rev. Lett. **90** (2003) 132301 [arXiv:nucl-th/0208001].

[66] R. J. Fries, B. Muller and D. K. Srivastava, arXiv:nucl-th/0507018.

[67] F. Arleo *et al.*, arXiv:hep-ph/0311131.

[68] R. Baier, Y. L. Dokshitzer, A. H. Mueller, S. Peigne and D. Schiff, Nucl. Phys. B **483** (1997) 291 [arXiv:hep-ph/9607355].

[69] K. Adcox *et al.* [PHENIX Collaboration], Phys. Rev. Lett. **88** (2002) 022301 [arXiv:nucl-ex/0109003].

[70] C. Adler *et al.* [STAR Collaboration], Phys. Rev. Lett. **89** (2002) 202301 [arXiv:nucl-ex/0206011].

[71] S. S. Adler *et al.* [PHENIX Collaboration], Phys. Rev. C **69** (2004) 034910 [arXiv:nucl-ex/0308006].

[72] J. Adams *et al.* [STAR Collaboration], Phys. Rev. Lett. **91** (2003) 172302 [arXiv:nucl-ex/0305015].

[73] B. B. Back *et al.* [PHOBOS Collaboration], Phys. Lett. B **578** (2004) 297 [arXiv:nucl-ex/0302015].

[74] I. Arsene *et al.* [BRAHMS Collaboration], Phys. Rev. Lett. **91** (2003) 072305 [arXiv:nucl-ex/0307003].

[75] K. J. Eskola, H. Honkanen, C. A. Salgado and U. A. Wiedemann, Nucl. Phys. A **747** (2005) 511 [arXiv:hep-ph/0406319].

[76] T. Hirano and Y. Nara, Phys. Rev. C **69** (2004) 034908 [arXiv:nucl-th/0307015].

[77] A. Bohr and B. R. Mottelson, Nuclear structure I, Benjamin, New York, 1969.

[78] K. J. Eskola and K. Tuominen, Phys. Lett. B **489** (2000) 329 [arXiv:hep-ph/0002008].

[79] K. J. Eskola and K. Tuominen, Phys. Rev. D **63** (2001) 114006 [arXiv:hep-ph/0010319].

[80] K. J. Eskola and K. Kajantie, Z. Phys. C **75** (1997) 515 [arXiv:nucl-th/9610015].

[81] P. Arnold, J. Lenaghan and G. D. Moore, JHEP **0308** (2003) 002 [arXiv:hep-ph/0307325].

[82] R. Baier, A. H. Mueller, D. Schiff and D. T. Son, Phys. Lett. B **502** (2001) 51 [arXiv:hep-ph/0009237].

[83] P. Huovinen, Nucl. Phys. A **715** (2003) 299 [arXiv:nucl-th/0210024].

[84] P. F. Kolb and R. Rapp, Phys. Rev. C **67** (2003) 044903 [arXiv:hep-ph/0210222].

[85] K. J. Eskola, K. Kajantie and K. Tuominen, Phys. Lett. B **497** (2001) 39 [arXiv:hep-ph/0009246].

[86] K. J. Eskola, K. Kajantie, P. V. Ruuskanen and K. Tuominen, Phys. Lett. B **543** (2002) 208 [arXiv:hep-ph/0204034].

[87] P. F. Kolb, J. Sollfrank and U. W. Heinz, Phys. Rev. C **62** (2000) 054909 [arXiv:hep-ph/0006129].

[88] T. S. Biro, E. van Doorn, B. Muller, M. H. Thoma and X. N. Wang, Phys. Rev. C **48** (1993) 1275 [arXiv:nucl-th/9303004].

[89] D. M. Elliott and D. H. Rischke, Nucl. Phys. A **671** (2000) 583 [arXiv:nucl-th/9908004].

[90] C. Adler *et al.* [STAR Collaboration], Phys. Rev. Lett. **87**, 112303 (2001) [nucl-ex/0106004].

[91] K. J. Eskola and H. Honkanen, Nucl. Phys. A **713** (2003) 167 [arXiv:hep-ph/0205048].

[92] I. Arsene *et al.* [BRAHMS Collaboration], Phys. Rev. Lett. **93** (2004) 242303 [arXiv:nucl-ex/0403005].

[93] [By PHOBOS Collaboration], arXiv:nucl-ex/0401006.

[94] T. Hirano and K. Tsuda, arXiv:nucl-th/0202033.

[95] D. Teaney, J. Lauret and E. V. Shuryak, arXiv:nucl-th/0110037.

[96] N. Armesto and C. Pajares, Int. J. Mod. Phys. A **15** (2000) 2019 [hep-ph/0002163].

[97] J. Ranft, arXiv:hep-ph/9911213.

[98] D. Kharzeev, E. Levin and M. Nardi, Nucl. Phys. A **747** (2005) 609 [arXiv:hep-ph/0408050].

[99] A. Accardi, Phys. Rev. C **64**, 064905 (2001) [hep-ph/0107301].

[100] S. S. Adler *et al.* [PHENIX Collaboration], Phys. Rev. Lett. **94** (2005) 232301 [arXiv:nucl-ex/0503003].

[101] C. Y. Wong and H. Wang, Phys. Rev. C **58** (1998) 376 [hep-ph/9802378].

[102] D. K. Srivastava and B. Sinha, Phys. Rev. C **64**, 034902 (2001) [nucl-th/0006018].

[103] D. Y. Peressounko and Y. E. Pokrovsky, arXiv:hep-ph/0009025.

[104] J. e. Alam, S. Sarkar, T. Hatsuda, T. K. Nayak and B. Sinha, Phys. Rev. C **63** (2001) 021901 [arXiv:hep-ph/0008074];
H. Arodz, M. Slusarczyk and A. Wereszczynski, Acta Phys. Polon. B **32** (2001) 2155 [arXiv:hep-ph/0106038].

[105] P. G. Jones *et al.* [NA49 Collaboration], Nucl. Phys. A **610** (1996) 188C.

[106] A. Dumitru, L. Frankfurt, L. Gerland, H. Stoecker and M. Strikman, Phys. Rev. C **64** (2001) 054909 [arXiv:hep-ph/0103203].

[107] See talks by H. Buesching, O. Drapier and S. Bathe at Quark Matter 2005, http://qm2005.kfki.hu/

[108] M. Strickland, Phys. Lett. B **331** (1994) 245.

[109] F. Gelis, K. Kajantie and T. Lappi, arXiv:hep-ph/0508229.